

# Heavy+light pseudoscalar meson semileptonic transitions

Zhen-Ni Xu<sup>a</sup>, Zhu-Fang Cui<sup>b</sup>, Craig D. Roberts<sup>c</sup>, Chang Xu<sup>d</sup>

<sup>1</sup> School of Physics, Nanjing University, Nanjing, Jiangsu 210093, China

<sup>2</sup> Institute for Nonperturbative Physics, Nanjing University, Nanjing, Jiangsu 210093, China

2021 March 28

**Abstract** A symmetry-preserving regularisation of a vector×vector contact interaction (SCI) is used to deliver a unified treatment of semileptonic transitions involving  $\pi$ ,  $K$ ,  $D_{(s)}$ ,  $B_{(s,c)}$  initial states. The framework is characterised by algebraic simplicity, few parameters, and the ability to simultaneously treat systems from Nambu-Goldstone modes to heavy+heavy mesons. Although the SCI form factors are typically somewhat stiff, the results are comparable with experiment and rigorous theory results. Hence, predictions for the five unmeasured  $B_{s,c}$  branching fractions should be a reasonable guide. The analysis provides insights into the effects of Higgs boson couplings via current-quark masses on the transition form factors; and results on  $B_{(s)} \rightarrow D_{(s)}$  transitions yield a prediction for the Isgur-Wise function in fair agreement with contemporary data.

## 1 Introduction

Pseudoscalar mesons are fascinating for many reasons. In the light-quark sector, the pion is remarkably light owing to dynamical chiral symmetry breaking [1]; itself, a corollary of emergent hadron mass (EHM) [2, 3]. Compared with the pion’s light  $u$ ,  $d$  quarks, the  $s$  quark in the  $K$  couples more strongly to the Higgs boson. Thus, the kaon is heavier. However, if these Higgs couplings are switched off, then the  $\pi$  and  $K$  are practically identical: they are Nature’s most fundamental Nambu-Goldstone bosons. Consequently, comparisons between pion and kaon properties provide information on empirical expressions of EHM and insights into the con-

structive interference between Nature’s two most basic mass generating mechanisms [4–9].

These observations are highlighted by studies of the leptonic and semileptonic decays of the  $\pi$  and  $K$ , which measure the scale of EHM, the strength of Higgs boson couplings into quantum chromodynamics (QCD), and the size of the entries in the Cabbibo-Kobayashi-Maskawa (CKM) matrix that generate the associated flavour-changing weak interactions. In these cases, the CKM matrix elements are  $|V_{ud}|$  and  $|V_{us}|$ . The former has been measured via the  $\pi^+ \rightarrow \pi^0 e^+ \nu_e$  transition [10], leading to [11, Sec. 12]:

$$|V_{ud}| = 0.9739(29). \quad (1)$$

The merits of this process lie in the facts that such semileptonic transitions proceed solely through the vector component of the weak interaction and there are no in-medium effects to consider, as there would be with measurements of nuclear transitions.

Semileptonic  $K$  decays are similarly used to extract  $|V_{us}|$ . In this case, the zero-recoil value of the dominant transition form factor is not unity, so the measurements constrain a product [11, Sec. 12]:

$$|V_{us}| f_+^{K\pi}(0) = 0.2165(4). \quad (2)$$

$f_+(0)$  can be calculated using continuum and lattice methods; and an average of modern lattice results yields [12]:  $f_+^{K\pi}(0) = 0.9706(27)$ ; hence,  $|V_{us}| = 0.2231(7)$ .

In connection with Eq. (2), an average of continuum predictions [13–15] yields

$$f_+^{K\pi}(0) = 0.972(8). \quad (3)$$

These Dyson-Schwinger equation (DSE) studies [16–19] employed the symmetry-preserving leading-order (rainbow-ladder, RL) truncation of the continuum bound-state problem [20, 21]; and no tuning effort was made.

<sup>a</sup>znxu@smail.nju.edu.cn

<sup>b</sup>phycui@nju.edu.cn

<sup>c</sup>cdroberts@nju.edu.cn

<sup>d</sup>cxu@nju.edu.cn

In combining them here, we exploited the fact that infrared observables are largely insensitive to the momentum dependence of the bound-state kernels owing to the emergence of a gluon mass-scale  $m_0 = 0.43(1)$  GeV [7, 22–25].

In the tower of flavoured pseudoscalar mesons, the next states are the  $D$  and  $D_s$ . The interplays between EHM and Higgs-boson (HB) mass generating effects in these systems are quite different from those in the lighter pseudoscalar mesons. Naturally,  $D$  and  $D_s$  would be indistinguishable from the  $\pi$  and  $K$  if all Higgs couplings were removed; but with the empirical values, the Higgs mechanism alone produces approximately 70% of their masses and constructive EHM+HB interference generates the remaining 30%, *i.e.* a 70:30 balance. The analogous results for the  $K$  and  $\pi$  are 20:80 and 5:95. Plainly, EHM is subdominant but still significant in  $D$  and  $D_s$  mesons.

These mass budgets were computed using information from Ref. [7, Figs. 1.1, 2.5], including predictions for the active masses of the  $c$  and  $b$  quarks at  $\zeta_2 = 2$  GeV, *viz.* 1.27 GeV and 4.18 GeV, respectively. Averages of lattice results produce the following values for these quantities [12]: 1.280(13), 4.198(12).

Precise data are available for  $D$  and  $D_s$  semileptonic decays [26–31]. They provide access to  $|V_{cd}|$  and  $|V_{cs}|$ ; albeit, once again, multiplied by soft form factors:  $f_+^{D_s K}(0)$ ,  $f_+^{D\pi}(0)$  and  $f_+^{DK}(0)$ . Lattice-QCD (lQCD) results are available for the last two [32] and continuum results for all three [15]:

$$\begin{array}{l} \left. \begin{array}{l} | \\ \text{continuum [15]} \\ \text{lattice [32]} \end{array} \right| \begin{array}{ccc} f_+^{D_s K}(0) & f_+^{D\pi}(0) & f_+^{DK}(0) \\ 0.673(40) & 0.618(31) & 0.756(36) \\ & 0.612(35) & 0.765(31) \end{array} \cdot \quad (4) \end{array}$$

A fourth form factor is not typically considered because the accuracy of isospin symmetry means  $D^+ \rightarrow \bar{K}^0$  and  $D^0 \rightarrow K^-$  are practically equivalent.

Including the  $b$  quark, one has three more pseudoscalar systems:  $B_c$ ,  $B_s$ ,  $B$ . In these cases, the HB *vs.* EHM+HB mass budgets are 87:13 for the  $B_c$  and 80:20 for  $B_s$ ,  $B$ . Plainly, the Higgs mechanism is dominant, but the role of EHM is persistently non-negligible. There are also many more possible semileptonic transitions:  $B_c \rightarrow B$  links with  $|V_{cd}|$ ;  $B_c \rightarrow B_s$  with  $|V_{cs}|$ ;  $B \rightarrow \pi$  and  $B_s \rightarrow K$  with  $|V_{ub}|$ ; and  $B \rightarrow D$ ,  $B_s \rightarrow D_s$ ,  $B_c \rightarrow \eta_c$  with  $|V_{cb}|$ . The last two open windows onto the third column of the CKM matrix. However, robust theoretical predictions for all the associated semileptonic transition form factors are difficult to obtain [33], owing chiefly to the vast separation between the masses of the participating valence-quarks and -antiquarks, and the diversity of competing scales in the processes.

The approach employed in Ref. [15] can be adapted to predicting the leptonic and semileptonic decays of mesons containing a  $b$  quark. In preparing for such a unifying study using realistic quark+antiquark interactions, it is helpful to have a benchmark. One is provided by calculations made with a symmetry-preserving formulation of a vector×vector contact interaction (SCI) [34, 35]. Such an approach preserves the character of more sophisticated treatments of the continuum bound-state problem whilst nevertheless enabling an algebraic simplicity; and widespread use has shown that, when interpreted carefully, SCI predictions provide a meaningful quantitative guide, see *e.g.* Refs. [36–48]. Thus, with SCI results in hand, one has the means to check the validity of algorithms employed in studies that rely (heavily) upon high performance computing.

This discussion is arranged as follows. Section 2 explains our implementation of the SCI, including constraint of the ultraviolet cutoff and determination of values for the interaction-dependent current-quark masses. Section 3 details the SCI treatment of semileptonic transitions that proceed via the weak vector vertex, using  $D \rightarrow \pi^-$  as the exemplar. Section 4 discusses SCI results for the three  $D_{(s)} \rightarrow \pi, K$  transitions that are distinguishable in the isospin-symmetry limit, including comparisons with other studies and experiment, where available. Section 5 proceeds with a similar discussion of the seven independent  $B_{(c,s)}$  semileptonic transitions, which present many challenges to experiment and theory [33]. Section 6 considers the question of environmental sensitivity, *i.e.* the evolution of semileptonic transition form factors as the Higgs mechanism of current-quark mass generation becomes a more important component of the final-state meson’s mass. Section 7 reports SCI predictions for the Isgur-Wise function [49], as inferred from the  $B_{(s)} \rightarrow D_{(s)}$  transitions. Section 8 presents a summary and perspective.

## 2 Contact Interaction

When studying the continuum meson bound-state problem, the primary element is the quark+antiquark scattering kernel. In RL truncation, it can be written ( $k = p_1 - p'_1 = p'_2 - p_2$ ,  $k^2 T_{\mu\nu}(k) = k^2 \delta_{\mu\nu} - k_\mu k_\nu$ ):

$$\mathcal{K}_{\alpha_1\alpha'_1,\alpha_2\alpha'_2} = \mathcal{G}_{\mu\nu}(k)[i\gamma_\mu]_{\alpha_1\alpha'_1}[i\gamma_\nu]_{\alpha_2\alpha'_2}, \quad (5a)$$

$$\mathcal{G}_{\mu\nu}(k) = \tilde{\mathcal{G}}(k^2)T_{\mu\nu}(k). \quad (5b)$$

The defining quantity is  $\tilde{\mathcal{G}}$ . Twenty years of study have revealed much about its pointwise behaviour. A key finding is that, owing to the emergence of a gluon mass-scale in QCD [7, 22–25],  $\tilde{\mathcal{G}}$  is nonzero and finite

at infrared momenta; so, one may write

$$\tilde{\mathcal{G}}(k^2) \stackrel{k^2 \approx 0}{\cong} \frac{4\pi\alpha_{\text{IR}}}{m_G^2}. \quad (6)$$

QCD has [25]:  $m_G \approx 0.5 \text{ GeV}$ ,  $\alpha_{\text{IR}} \approx \pi$ . We follow Ref. [46], retaining this value of  $m_G$ , and since the SCI cannot support relative momentum between bound-state constituents, simplifying the tensor structure in Eqs. (5) such that, in operation:

$$\mathcal{K}_{\alpha_1\alpha'_1,\alpha_2\alpha'_2}^{\text{CI}} = \frac{4\pi\alpha_{\text{IR}}}{m_G^2} [i\gamma_\mu]_{\alpha_1\alpha'_1} [i\gamma_\mu]_{\alpha_2\alpha'_2}. \quad (7)$$

We implement a rudimentary form of confinement in the SCI by introducing an infrared regularisation scale,  $\Lambda_{\text{ir}}$ , when defining bound-state equations [50]. This device excises momenta less than  $\Lambda_{\text{ir}}$ , so eliminating quark+antiquark production thresholds [51]. The usual choice is  $\Lambda_{\text{ir}} = 0.24 \text{ GeV}$  [35].

At the other extreme, the integrals appearing in SCI bound-state equations require ultraviolet regularisation. This breaks the link between infrared and ultraviolet scales that is a feature of QCD. The ultraviolet mass-scales,  $\Lambda_{\text{uv}}$ , become physical parameters that may be interpreted as upper bounds on the momentum domains whereupon distributions within the associated systems are effectively momentum-independent. For instance, the  $\pi$ -meson is larger in size than the  $B$ -meson; hence, one should expect  $1/\Lambda_{\text{uv}}^\pi > 1/\Lambda_{\text{uv}}^B$ . As subsequently explained, this observation leads us to a completion of the SCI through introduction of a scale-dependent coupling [43–46].

The SCI gap equation for a quark of flavour  $f$  is

$$S_f^{-1}(p) = i\gamma \cdot p + m_f + \frac{16\pi}{3} \frac{\alpha_{\text{IR}}}{m_G^2} \int \frac{d^4q}{(2\pi)^4} \gamma_\mu S_f(q) \gamma_\mu, \quad (8)$$

where  $m_f$  is the quark's current-mass. Using a Poincaré-invariant regularisation, the solution is

$$S_f(p)^{-1} = i\gamma \cdot p + M_f, \quad (9)$$

with  $M_f$  obtained by solving

$$M_f = m_f + M_f \frac{4\alpha_{\text{IR}}}{3\pi m_G^2} C_0^{\text{iu}}(M_f^2), \quad (10)$$

where

$$C_0^{\text{iu}}(\sigma) = \int_0^\infty ds s \int_{\tau_{\text{uv}}^2}^{\tau_{\text{ir}}^2} d\tau e^{-\tau(s+\sigma)} = \sigma [\Gamma(-1, \sigma\tau_{\text{uv}}^2) - \Gamma(-1, \sigma\tau_{\text{ir}}^2)]. \quad (11)$$

$\Gamma(\alpha, y)$  is the incomplete gamma-function. In general, functions of the following form arise in solving SCI bound-state equations ( $\tau_{\text{uv}}^2 = 1/\Lambda_{\text{uv}}^2$ ,  $\tau_{\text{ir}}^2 = 1/\Lambda_{\text{ir}}^2$ ):

$$\bar{C}_n^{\text{iu}}(\sigma) = \Gamma(n-1, \sigma\tau_{\text{uv}}^2) - \Gamma(n-1, \sigma\tau_{\text{ir}}^2), \quad (12)$$

$$C_n^{\text{iu}}(\sigma) = \sigma \bar{C}_n^{\text{iu}}(\sigma), \quad n \in \mathbb{Z}^{\geq}.$$

Pseudoscalar ( $J^P = 0^-$ ) mesons emerge as quark+antiquark bound-states. They are described by a Bethe-Salpeter amplitude, whose SCI form is [14]:

$$\Gamma_{0^-}(Q) = \gamma_5 \left[ iE_{0^-}(Q) + \frac{1}{2M_{fg}} \gamma \cdot Q F_{0^-}(Q) \right], \quad (13)$$

$M_{fg} = M_f M_g / [M_f + M_g]$ ,  $Q$  is the bound-state's total momentum,  $Q^2 = -m_{0^-}^2$ ,  $m_{0^-}$  is the meson's mass.

The amplitude and  $m_{0^-}^2$  are obtained by solving the following Bethe-Salpeter equation: ( $t_+ = t + Q$ ):

$$\Gamma_{0^-}(Q) = -\frac{16\pi}{3} \frac{\alpha_{\text{IR}}}{m_G^2} \times \int \frac{d^4t}{(2\pi)^4} \gamma_\mu S_f(t_+) \Gamma_{0^-}(Q) S_g(t) \gamma_\mu. \quad (14)$$

Our symmetry-preserving approach implements a dimensional-regularisation-like identity [14]:

$$0 = \int_0^1 d\alpha [C_0^{\text{iu}}(\omega_{fg}(\alpha, Q^2)) + C_1^{\text{iu}}(\omega_{fg}(\alpha, Q^2))], \quad (15)$$

where ( $\hat{\alpha} = 1 - \alpha$ )

$$\omega_{fg}(\alpha, Q^2) = M_f^2 \hat{\alpha} + \alpha M_g^2 + \alpha \hat{\alpha} Q^2. \quad (16)$$

Using Eq. (15), one arrives at the following Bethe-Salpeter equation:

$$\begin{bmatrix} E_{0^-}(Q) \\ F_{0^-}(Q) \end{bmatrix} = \frac{4\alpha_{\text{IR}}}{3\pi m_G^2} \begin{bmatrix} \mathcal{K}_{EE}^{0-} & \mathcal{K}_{EF}^{0-} \\ \mathcal{K}_{FE}^{0-} & \mathcal{K}_{FF}^{0-} \end{bmatrix} \begin{bmatrix} E_{0^-}(Q) \\ F_{0^-}(Q) \end{bmatrix}, \quad (17)$$

with

$$\mathcal{K}_{EE}^{0-} = \int_0^1 d\alpha \left\{ C_0^{\text{iu}}(\omega_{fg}(\alpha, Q^2)) + \left[ M_f M_g - \alpha \hat{\alpha} Q^2 - \omega_{fg}(\alpha, Q^2) \right] \times \bar{C}_1^{\text{iu}}(\omega_{fg}(\alpha, Q^2)) \right\}, \quad (18a)$$

$$\mathcal{K}_{EF}^{0-} = \frac{Q^2}{2M_{fg}} \int_0^1 d\alpha \left[ \hat{\alpha} M_f + \alpha M_g \right] \times \bar{C}_1^{\text{iu}}(\omega_{fg}(\alpha, Q^2)), \quad (18b)$$

$$\mathcal{K}_{FE}^{0-} = \frac{2M_{fg}^2}{Q^2} \mathcal{K}_{EF}^{0-}, \quad (18c)$$

$$\mathcal{K}_{FF}^{0-} = -\frac{1}{2} \int_0^1 d\alpha \left[ M_f M_g + \hat{\alpha} M_f^2 + \alpha M_g^2 \right]$$

**Table 1** Couplings, ultraviolet cutoffs and current-quark masses that deliver a good description of flavoured pseudoscalar meson properties, along with the dressed-quark masses and chosen pseudoscalar meson properties they produce; all obtained with  $m_G = 0.5 \text{ GeV}$ ,  $A_{\text{ir}} = 0.24 \text{ GeV}$ . Empirically, at a sensible level of precision [11]:  $m_\pi = 0.14$ ,  $f_\pi = 0.092$ ;  $m_K = 0.50$ ,  $f_K = 0.11$ ;  $m_D = 1.87$ ,  $f_D = 0.15$ ;  $m_B = 5.30$ ,  $f_B = 0.14$ . (Dimensioned quantities in GeV.)

	quark	$\alpha_{\text{IR}}/\pi$	$\Lambda_{\text{uv}}$	$m$	$M$	$m_{0^-}$	$f_{0^-}$
$\pi$	$l = u/d$	0.36	0.91	0.007	0.37	0.14	0.10
$K$	$\bar{s}$	0.33	0.94	0.16	0.53	0.50	0.11
$D$	$c$	0.12	1.36	1.39	1.57	1.87	0.15
$B$	$\bar{b}$	0.052	1.92	4.81	4.81	5.30	0.14

$$\times \bar{C}_1^{\text{iu}}(\omega_{fg}(\alpha, Q^2)). \quad (18d)$$

The value of  $Q^2 = -m_{0^-}^2$  for which Eq. (17) is satisfied supplies the bound-state mass and the associated solution vector is the meson’s Bethe-Salpeter amplitude. In the calculation of observables, the canonically normalised amplitude must be used, *viz.* the amplitude obtained after rescaling such that

$$1 = \frac{d}{dQ^2} \Pi_{0^-}(Z, Q) \Big|_{Z=Q}, \quad (19)$$

where, with the trace over spinor indices:

$$\Pi_{0^-}(Z, Q) = 6 \text{tr}_D \int \frac{d^4 t}{(2\pi)^4} \times \Gamma_{0^-}(-Z) S_f(t_+) \Gamma_{0^-}(Z) S_g(t). \quad (20)$$

In terms of the canonically normalised Bethe-Salpeter amplitude, the pseudoscalar meson’s leptonic decay constant is

$$f_{0^-} = \frac{N_c}{4\pi^2} \frac{1}{M_{fg}} [E_0 - \mathcal{K}_{FE}^{0^-} + F_0 - \mathcal{K}_{FF}^{0^-}]_{Q^2 = -m_{0^-}^2}. \quad (21)$$

The properties of  $\pi^-$  and  $\rho^-$  mesons were analysed in Ref. [35], with the optimal description provided by the parameters and associated current-quark mass in the middle columns of Table 1, row 1. The last three columns report calculated results for the dressed  $u$ -quark mass, pion mass and pion decay constant.

Keeping the light-quark values, we determined the  $s$ -quark current mass,  $m_s$ , and  $K$ -meson ultraviolet cutoff,  $\Lambda_{\text{uv}}^K$ , through a least-squares fit to empirical values of  $m_K$ ,  $f_K$  whilst imposing the relation:

$$\alpha_{\text{IR}}(\Lambda_{\text{uv}}^K) [\Lambda_{\text{uv}}^K]^2 \ln \frac{\Lambda_{\text{uv}}^K}{\Lambda_{\text{ir}}} = \alpha_{\text{IR}}(\Lambda_{\text{uv}}^\pi) [\Lambda_{\text{uv}}^\pi]^2 \ln \frac{\Lambda_{\text{uv}}^\pi}{\Lambda_{\text{ir}}}. \quad (22)$$

This procedure eliminates one parameter by implementing the physical constraint that any increase in the

**Table 2** Computed masses, Bethe-Salpeter amplitudes, and decay constants for a representative selection of mesons. Empirical masses from Ref. [11]; entry marked by “\*” from Ref. [53]. Empirically unknown decay constants quoted from lQCD [12, 54–56]. (Dimensioned quantities in GeV. Underlined entries from Table 1.)

$J^P$	Meson	$m^{\text{CI}}$	$m^{e/1}$	$E$	$F$	$f^{\text{CI}}$	$f^{e/1}$
$0^-$	$\pi(u\bar{d})$	<u>0.14</u>	0.14	3.59	0.47	<u>0.10</u>	0.092
	$K(u\bar{s})$	<u>0.50</u>	0.50	3.70	0.55	<u>0.11</u>	0.11
	$D(u\bar{c})$	<u>1.87</u>	1.87	3.25	0.39	0.15	0.15(1)
	$D_s(s\bar{c})$	1.96	1.97	3.45	0.54	0.16	0.18
	$\eta_c(c\bar{c})$	2.90	2.98	3.74	0.90	0.20	0.24(1)
	$B(u\bar{b})$	<u>5.30</u>	5.30	2.98	0.18	<u>0.14</u>	0.13
	$B_s(s\bar{b})$	5.38	5.37	3.26	0.27	0.16	0.16
	$B_c(c\bar{b})$	6.16	6.28	4.25	0.79	0.21	0.35
$1^-$	$K^*(u\bar{s})$	1.10	0.89	1.31		0.15	0.16
	$D^*(u\bar{c})$	2.09	2.01	1.25		0.15	0.17(1)
	$D_s^*(s\bar{c})$	2.18	2.11	1.30		0.15	0.19(1)
	$B^*(u\bar{b})$	5.36	5.33	1.26		0.13	0.13(2)
	$B_s^*(s\bar{b})$	5.45	5.42	1.34		0.14	0.16(2)
	$B_c^*(c\bar{b})$	6.24	6.33*	1.97		0.20	0.34(2)

momentum-space extent of a hadron wave function is matched by a reduction in the effective coupling between the constituents. Critical over-binding is thus avoided. The results are listed in Table 1, row 2. The procedure is repeated for the  $c$ -quark/ $D$ -meson and  $\bar{b}$ -quark/ $B$ -meson, with results in Table 1, rows 3, 4.

Regarding the current-quark masses in Table 1, the fitted value of  $m_s/m_l = 24$  matches estimates in QCD [11], despite the individual current-masses being too large by a factor of  $\lesssim 2$  because the SCI is deficient in connection with ultraviolet quantities. The result  $M_s/M_l = 1.4$  is a fair match with the value determined in efficacious RL studies with momentum-dependent interactions [52]:  $M_s/M_l = 1.25(9)$ . Similarly, the results for  $m_c$ ,  $m_b$  are individually somewhat higher than QCD estimates, but the values for  $M_{c,b}$  are commensurate with typical values of the heavy-quark pole masses [11]. This is the character of the SCI: it is not a precision tool; but when employed judiciously, it is qualitatively and semiquantitatively reliable.

The evolution of the ultraviolet cutoff with pseudoscalar meson mass reported in Table 1 is described by the following interpolation ( $s = m_{0^-}^2$ ):

$$\Lambda_{\text{uv}}(s) = 0.306 \ln[19.2 + (s/m_\pi^2 - 1)/2.70]. \quad (23)$$

For a given meson,  $H$ , the associated coupling can then be obtained using Eq. (22), with  $[\Lambda_{\text{uv}}^K]^2 \rightarrow m_H^2 = s$ . One can subsequently compute properties of any meson for which a mass estimate is available by solving the associated Bethe-Salpeter equation with the prescribed cutoff and coupling, using the dressed-quark propagators already determined. Proceeding as described here, one

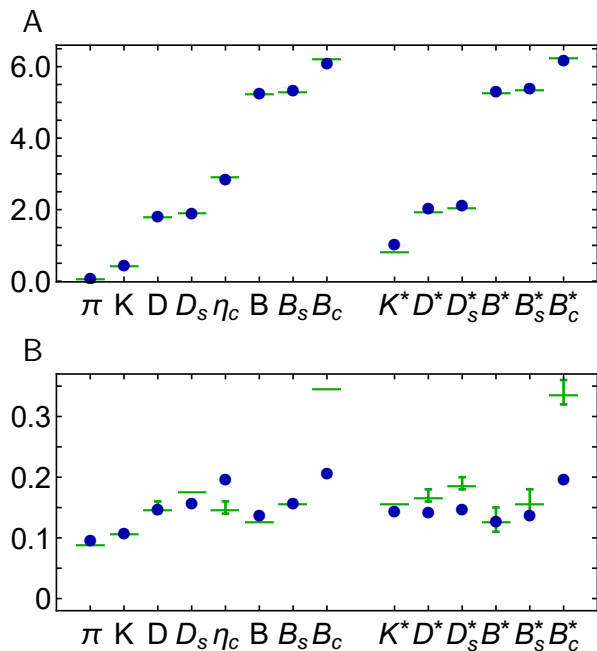


**Fig. 1** *Upper panel*–A. Comparison between CI predictions for selected meson masses and available experiment [11] and  $m_{B_c^*}$  from Ref. [53]. *Lower panel*–B. Analogous comparison for meson leptonic decay constants: experiment [11], where known, and IQCD otherwise [12, 54–56]. In both panels, contact-interaction predictions are depicted as blue circles and comparison values by green bars. (Pictorial representation of results in Table 2.)

obtains the meson masses and decay constants listed in Table 2.

As highlighted in Fig. 1A, SCI results for the masses are in good agreement with experiment: the mean absolute relative difference  $\overline{\text{ard}} = 2.8\%$ . Particularities associated with ensuring the vector Ward-Green-Takahashi identity entail that the description is better for pseudoscalars than it is for vector mesons [34].

Regarding the leptonic decay constants, Fig. 1B, the SCI supplies a poorer description because these observables describe quark+antiquark annihilation at a single spacetime point. Hence, they are sensitive to ultraviolet physics, which is a challenge for the SCI. Eqs. (22), (23) are useful in repairing the deficiency. They ensure that in comparison with known empirical values or available IQCD results, the picture is fair: trends are typically reproduced; and comparing columns 6 and 7 in Table 2,  $\overline{\text{ard}} = 13\%$ . The discrepancies between SCI and IQCD results for  $f_{B_c}$ ,  $f_{B_c^*}$  appear anomalously large. Eliminating them, then  $\overline{\text{ard}} = 8.3\%$ . However, although the IQCD results were obtained some time ago [55], they are consistent with modern continuum predictions developed using realistic interactions [57].

It should be noted that our ultraviolet improvement scheme differs from that in Ref. [46]. Therein, pseu-

doscalar mesons with mass-degenerate valence degrees-of-freedom were used to develop a running scale like that in Eq. (23). Owing to our subsequent focus on semileptonic decays of flavoured pseudoscalar mesons, we instead used the underlined masses in Table 2.

### 3 Semileptonic Transitions: Foundations

#### 3.1 Matrix Elements

Our SCI analysis of pseudoscalar meson semileptonic decays follows the treatment of  $K_{\ell 3}$  transitions in Ref. [14]. We will sketch the procedure using the  $D^0 \rightarrow \pi^-$  transition. All others can be developed by analogy. Therefore, consider the following matrix element:<sup>1</sup>

$$\begin{aligned} {}_d M_\mu^{D^0}(P, Q) &= \langle \pi^-(p) | \bar{d} i \gamma_\mu c | D^0(k) \rangle \\ &= [P_\mu f_+^{D^d}(t) + Q_\mu f_-^{D^d}(t)], \end{aligned} \quad (24)$$

where  $P = k + p$ ,  $Q = p - k$ , with  $k^2 = -m_D^2$  and  $p^2 = -m_\pi^2$ , and the squared-momentum-transfer is  $t = -Q^2$ .

The masses of the hadrons involved limit the physical domain of support for the form factors:

$$P \cdot Q = -(m_D^2 - m_\pi^2) =: -\Delta_{D\pi}, \quad (25a)$$

$$P^2 = -2(m_D^2 + m_\pi^2) - Q^2 =: -2\Sigma_{D\pi} - Q^2; \quad (25b)$$

and  $t_m^{D\pi} = (m_D - m_\pi)^2 =: m_D^2 y_m^{D\pi}$  is the largest value of the squared-momentum-transfer in the decay process.

In the flavour-symmetry limit,  $f_+^D(t)$  is equivalent to the elastic form factor of a charged pion-like meson built from a valence-quark and -antiquark with degenerate current masses and  $f_-^D(t) \equiv 0$  [58]. In all transitions, therefore,  $f_-(t)$  is sensitive to the strength of HB-induced flavour-symmetry breaking, as are various sensibly constructed ratios of  $f_+$  transition form factors, e.g.  $D^+ \rightarrow K^0$  vs.  $D^0 \rightarrow \pi^-$  reflects  $s$ -quark: $u$ -quark differences. These properties are correlated with the scalar form factor

$$f_0^D(t) = f_+^D(t) + \frac{t}{m_D^2 - m_\pi^2} f_-^D(t), \quad (26)$$

and its analogues, which all measure the divergence of the transition current,  $Q \cdot M(P, Q)$ .

The additional merit of focusing on  $f_{+,0}(t)$  is that each is characterised by a different resonance structure on  $t \gtrsim t_m$ :  $f_+(t)$  links with the vector meson  $D^*$ ; and  $f_0(t)$  with the related scalar resonance. On the other hand,  $f_-(t)$  overlaps with both channels. (These observations are exemplified in Refs. [13–15] and below.)

<sup>1</sup>Euclidean metric conventions:  $\{\gamma_\mu, \gamma_\nu\} = 2\delta_{\mu\nu}$ ;  $\gamma_\mu^\dagger = \gamma_\mu$ ;  $\gamma_5 = \gamma_4 \gamma_1 \gamma_2 \gamma_3$ ,  $\text{tr}[\gamma_5 \gamma_\mu \gamma_\nu \gamma_\rho \gamma_\sigma] = -4\epsilon_{\mu\nu\rho\sigma}$ ;  $\sigma_{\mu\nu} = (i/2)[\gamma_\mu, \gamma_\nu]$ ;  $a \cdot b = \sum_{i=1}^4 a_i b_i$ ; and  $Q_\mu$  timelike  $\Rightarrow Q^2 < 0$ .

Using our SCI, the matrix element in Eq. (24) takes the following explicit form:

$${}_dM_\mu^{D^0}(P, Q) = N_c \text{tr} \int \frac{d^4t}{(2\pi)^4} \Gamma_D(p) S_c(t+p) \times i\Gamma_\mu^{cd}(Q) S_d(t+k) \Gamma_\pi(-k) S_u(t), \quad (27)$$

where the trace is over spinor indices and  $N_c = 3$ . The scalar functions characterising the transition are obtained from Eq. (27) using straightforward projections:

$$f_+^{D^d}(t) = \frac{tP_\mu - (m_D^2 - m_\pi^2)Q_\mu}{tP^2 + (m_D^2 - m_\pi^2)^2} {}_dM_\mu^{D^0}(P, Q), \quad (28a)$$

$$f_0^{D^d}(t) = -\frac{Q_\mu}{m_D^2 - m_\pi^2} {}_dM_\mu^{D^0}(P, Q), \quad (28b)$$

with  $f_-^{D^d}(t)$  reconstructed via Eq. (26).

Three types of matrix-valued functions appear in Eq. (27). Simplest are the dressed-quark propagators, which have the form in Eq. (9) and involve the appropriate dressed-quark mass drawn from Table 1. Next are the Bethe-Salpeter amplitudes for the participating mesons, whose structure is given in Eq. (13) and which are also completed by the numerical results in Table 1. The new element is the dressed vector component of, in this instance, the  $c \rightarrow d$  weak transition vertex,  $\Gamma_\mu^{cd}$ . Other transitions involve an analogous vector vertex.

### 3.2 Weak Vector Vertex

The vector component of the  $c \rightarrow d$  weak transition vertex satisfies a Ward-Green-Takahashi identity:

$$Q_\mu i\Gamma_\mu^{cd}(Q) = S_c^{-1}(t+Q) - S_d^{-1}(t) - (m_c - m_d)\Gamma_I^{cd}(Q), \quad (29)$$

where  $\Gamma_I^{cu}$  is an analogous Dirac-scalar vertex. Recall that the axial-vector piece of the quark weak vertex does not contribute to a  $0^- \rightarrow 0^-$  transition. As with all  $n$ -point functions, care must be taken when formulating the SCI solution procedure for this vertex; so, it is worth providing some details.

The two vertices in Eq. (29) satisfy inhomogeneous Bethe-Salpeter equations, *viz.* in RL truncation:

$$\Gamma_\mu^{cd}(Q) = \gamma_\mu - \frac{16}{3} \frac{\pi\alpha_{\text{IR}}}{m_G^2} \times \int \frac{d^4t}{(2\pi)^4} \gamma_\alpha S_c(t+Q) \Gamma_\mu^{cd}(Q) S_d(t) \gamma_\alpha, \quad (30a)$$

$$\Gamma_I^{cu}(Q) = I_D - \frac{16}{3} \frac{\pi\alpha_{\text{IR}}}{m_G^2} \times \int \frac{d^4t}{(2\pi)^4} \gamma_\alpha S_c(t+Q) \Gamma_I^{su}(Q) S_d(t) \gamma_\alpha. \quad (30b)$$

So long as the regularisation scheme is symmetry preserving, then the solutions are

$$\Gamma_\mu^{cd}(Q) = \gamma_\mu^T P_T^{cd}(Q^2) + \gamma_\mu^L P_{1L}^{cd}(Q^2) - iQ_\mu I_D P_{2L}^{cd}(Q^2), \quad (31a)$$

$$\Gamma_I^{cd}(Q) = I_D E_I^{cd}(Q^2), \quad (31b)$$

where  $I_D$  is the identity matrix in spinor space,  $Q_\mu \gamma_\mu^T = 0$ ,  $\gamma_\mu^T + \gamma_\mu^L = \gamma_\mu$ .

Following Ref. [14], one finds:

$$E_I^{cd}(Q^2) = \frac{1}{1 + K_E^{cd}(Q^2)}, \quad (32a)$$

where

$$K_E^{cd}(Q^2) = -\frac{4\alpha_{\text{IR}}}{3\pi m_G^2} \int_0^1 d\alpha \left[ \mathcal{C}^{\text{iu}}(w_{d\bar{c}}) - \mathcal{C}_1^{\text{iu}}(w_{d\bar{c}}) - (M_d M_c + \alpha \hat{\alpha} Q^2) \bar{\mathcal{C}}_1^{\text{iu}}(w_{d\bar{c}}) \right], \quad (32b)$$

$w_{d\bar{c}} = \omega_{d\bar{c}}(\alpha, Q^2)$ , Eq. (16), and the other functions are defined via Eq. (12). It is apparent under further inspection that  $E_I^{cd}(Q^2)$  exhibits a pole at the mass of the lightest  $0^+ \bar{c}d$  state, *i.e.* the  $D_0^*$ -meson. Furthermore,

$$(m_c - m_d)E_I^{cd}(Q^2 = 0) = M_c - M_d. \quad (33)$$

It is worth remarking that owing to uncertainties in the spectrum of heavy+light  $0^+$  mesons, the coupling and ultraviolet cutoff in Eq. (32b) are fixed using Eqs. (22), (23) evaluated at the mass of the ground-state pseudoscalar meson in the given channel; here,  $m_D$ . As noted above, ultraviolet cutoffs play a dynamical role in the formulation of a contact interaction; so, this choice is merely part of the definition of the symmetry-preserving regularisation scheme. Given that it is a scalar channel, the value of the ultraviolet cutoff feeds back through Eq. (33) into small variations of the current-quark masses so that the dressed-quark masses remain fixed.

Turning to Eq. (30a), one readily finds [14]

$$P_{1L}^{cd}(Q^2) \equiv 1; \quad (34)$$

and

$$P_T^{cd}(Q^2) = \frac{1}{1 + K_V^{cd}(Q^2)}, \quad (35)$$

$$K_V^{cd}(Q^2) = -\frac{2\alpha_{\text{IR}}}{3\pi m_G^2} \int_0^1 d\alpha [M_d M_c - M_d^2 \hat{\alpha} - M_c^2 \alpha - 2\alpha \hat{\alpha} Q^2] \bar{\mathcal{C}}_1^{\text{iu}}(w_{d\bar{c}}). \quad (36)$$

The transverse part of this quark weak vector vertex has a pole at the mass of the  $D^*$ -meson.

Considering Eq. (31a), only  $P_{2L}^{cd}(Q^2)$  remains undetermined. Adapting the analysis in Ref. [14], one obtains

$$Q^2 P_{2L}^{cd}(Q^2) = (m_d - m_c) E_T^{cd}(Q^2) - M_d + M_c. \quad (37)$$

Using Eq. (33), it is clear that  $\lim_{Q^2 \rightarrow 0} Q^2 P_{2L}^{cd}(Q^2) = 0$ ; consequently,  $\Gamma_\mu^{cd}(Q)$  is regular at  $Q^2 = 0$ .

Our attempt to achieve a symmetry-preserving calculation of the quark weak vector vertex has almost succeeded. One issue remains; namely, consistency between Eqs. (9), (29), (33) requires

$$P_T^{cd}(Q^2 = 0) = 1. \quad (38)$$

Considering the ten transitions considered herein, our scheme fails by 2.4(1.5)%. We subsequently correct for this by modifying the denominator in Eq. (35):

$$K_V^{cd}(Q^2) \rightarrow \hat{K}_V^{cd}(Q^2) := K_V^{cd}(Q^2) - K_V^{cd}(0), \quad (39)$$

with analogous corrections in the other vertices. This is akin to implementing momentum-subtraction regularisations of the vector-boson vacuum polarisations.

### 3.3 Charge Conservation

In working from Eq. (27) to explicit expressions for  $f_+^{D_u^d}(t)$ ,  $f_0^{D_u^d}(t)$ , one follows the methods in Refs. [35]. They rely chiefly on the assumption of Poincaré-invariance, including translational invariance in regularisation of the integrals. Formally, the latter is always true. However, the presence of the  $\gamma_5 \gamma \cdot Q$  term in Eq. (13) means it is broken in practice once Eq. (11) is used. This violation is manifest in the elastic electromagnetic form factors of the pseudoscalar mesons that participate in the transitions, as we now explain.

Elastic form factors obtained using the SCI can be expressed as a sum of six terms. The first separation stems from the photon coupling either to the quark ( $\gamma q$ ) or the antiquark ( $\gamma \bar{q}$ ). It is the same for all quark+antiquark interactions. When using the SCI, there are three subcomponents in each of these two terms. Namely, the Bethe-Salpeter amplitude in Eq. (13) leads to  $E_{0-}^2$ ,  $E_{0-} F_{0-}$ ,  $F_{0-}^2$  contributions. The  $F_{0-}^2$  term vanishes at  $Q^2 = 0$  and the  $E_{0-}^2$  is insensitive to the regularisation. However, following the regularisation steps described hitherto

$$\langle E_{0-} F_{0-} \rangle |_{Q^2=0}^{\gamma q} \neq \langle E_{0-} F_{0-} \rangle |_{Q^2=0}^{\gamma \bar{q}}, \quad (40)$$

*i.e.* these two contributions are not equal and that violates charge conservation. Typically, the relative error is  $\lesssim 1\%$ , but it should vanish.

The mismatch owes to the quadratic divergences that arise through integrals such as

$$\begin{aligned} & \int \frac{d^4 t}{(2\pi)^4} \frac{1}{[t^2 + \omega]^2} \{(P \cdot t)^2, (Q \cdot t)^2, (P \cdot t)(Q \cdot t)\} \\ &= \int \frac{d^4 t}{(2\pi)^4} \frac{t^2}{[t^2 + \omega]^2} \frac{1}{4} \{P^2, Q^2, P \cdot Q\}, \end{aligned} \quad (41)$$

which also affect the value of  $f_+^{H_1 H_2}(0)$ . It can be remedied through a simple expedient: change

$$\frac{1}{4} \rightarrow \frac{1}{4} (1 + \theta) \quad (42)$$

and tune  $\theta$  to restore equality of the two sides in Eq. (40). We have computed  $\theta$  from the elastic form factor of every one of the initial states in the transitions considered herein:  $D_{(s)}$ ,  $B_{(s,c)}$ , with the results  $\theta = 0.28, 0.40, 0.01, 0.18, 0.17$ . (Evidently, the mismatch is eliminated by choosing  $\theta \approx 0.21$ .) These values are used to complete the regularisation of the transition form factors specified by Eq. (27) and its analogues.

Before delivering new SCI predictions, it is worth remarking that we have confirmed all results in Ref. [14], including those connected with  $K_{\ell 3}$  and  $\pi_{e 3}$  transitions.

### 4 Weak $D_{(s)}$ Semileptonic Transitions

In the isospin-symmetry limit, there are three distinct such processes:  $D^0 \rightarrow \pi^-$ ,  $D_s^+ \rightarrow K^0$ ,  $D^+ \rightarrow \bar{K}^0$ . The first two measure  $c \rightarrow d$  and the last,  $c \rightarrow s$ ; and all provide information on the environmental sensitivity of these transitions. These transitions were calculated using a realistic quark+antiquark interaction in Ref. [15]; so, comparison here serves to establish the utility of the SCI as a quantitative guide in such applications.

Results for the maximum-recoil value of the transition form factors are listed in Table 3A. Taken over all quantities listed in the first three rows, the  $F_{0-} \neq 0$  SCI results provide a better match with Ref. [15].

The SCI  $D \rightarrow \pi$  transition form factors are depicted in Fig. 2 and compared with analogous form factors drawn from Ref. [15]. On balance, best agreement is obtained using the SCI results produced with the complete Bethe-Salpeter amplitudes. It is worth recalling that the  $D \rightarrow \pi$  semileptonic transition form factors calculated in Ref. [15] are in good agreement with available empirical data [28].

A general characteristic of SCI form factors is evident in Fig. 2; namely, they are typically stiffer than predictions obtained with realistic momentum-dependent interactions [14]. This is more of an issue with their spacelike behaviour. It is ameliorated herein because our focus is the timelike region and, as demonstrated in Sec. 3.2, the SCI preserves the feature that

**Table 3** *Upper panel*–A. Maximum recoil ( $t = 0$ ) value of semileptonic transition form factors compared with (where available) inferences from experiment [28, 29] and IQCD [12, 59–61]. In each case, we list results for  $f_+^{H_1 \rightarrow H_2}(0)$  obtained with (column 1) the complete SCI Bethe-Salpeter amplitude, Eq. (13), and (column 2) with  $F_{0^-} \rightarrow 0$  and all procedures repeated. Comparison between these columns provides an indication of the sensitivity in SCI predictions to formulation details. Our analogous predictions for  $f_-^{H_1 \rightarrow H_2}(t = 0)$  are listed in columns 6 and 7. *Lower panel*–B. SCI computed branching fractions (columns 1, 2), obtained using empirical masses, compared with, where available: continuum results from Ref. [15] (column 3); empirical results (column 4) [11, 28, 29, 62]; IQCD (column 5) [61]; and illustrative model analyses (column 6) [63–66]. (All numerical entries should be multiplied by  $10^{-3}$ .) Ref. [11] lists  $|V_{cd}| = 0.221(4)$ ,  $|V_{cs}| = 0.987(11)$ ,  $|V_{ub}| = 0.00382(24)$ ,  $|V_{cb}| = 0.0410(14)$ ; and the following lifetimes (in seconds):  $\tau_{D^0} = 4.10 \times 10^{-13}$ ,  $\tau_{D_s^\pm} = 5.04 \times 10^{-13}$ ,  $\tau_{B^0} = 1.519 \times 10^{-12}$ ,  $\tau_{B_s^0} = 1.515 \times 10^{-12}$ ,  $\tau_{B_c^\pm} = 5.10 \times 10^{-13}$ .

A. $f_+(0)$	here $_{F_{0^-} \neq 0}$	here $_{F_{0^-} = 0}$	Ref. [15]	expt.	IQCD	here $_{F_{0^-} \neq 0}^{ f_-(0) }$	here $_{F_{0^-} = 0}^{ f_-(0) }$	Ref. [15] $_{ f_-(0) }$
1 $D \rightarrow \pi$	0.76	0.65	0.618(31)	0.637(09)	0.612(35)	0.35	0.54	0.362(28)
2 $D_s \rightarrow K$	0.75	0.65	0.673(40)	0.720(85)		0.35	0.55	0.553(65)
3 $D \rightarrow K$	0.81	0.72	0.756(36)	0.737(04)	0.765(31)	0.33	0.50	0.277(45)
4 $B \rightarrow \pi$	0.57	0.48			0.169(51)	0.38	0.48	
5 $B_s \rightarrow K$	0.53	0.43			0.281(12)	0.36	0.45	
6 $B \rightarrow D$	0.75	0.72			0.818(22)	0.40	0.45	
7 $B_s \rightarrow D_s$	0.74	0.71			0.666(12)	0.39	0.45	
8 $B_c \rightarrow \eta_c$	0.73	0.61			$\approx 0.6$	0.40	0.43	
9 $B_c \rightarrow B$	0.68	0.67			0.55(2)	0.49	0.71	
10 $B_c \rightarrow B_s$	0.75	0.75			0.62(1)	0.55	0.79	

B.	here $_{F_{0^-} \neq 0}$	here $_{F_{0^-} = 0}$	Ref. [15]	expt.	IQCD	model
1 $\mathcal{B}_{D^0 \rightarrow \pi^- e^+ \nu_e}$	2.96	2.57	2.73(22)	2.95(05)		
2 $\mathcal{B}_{D_s^+ \rightarrow K^0 e^+ \nu_e}$	2.83	2.40	3.31(33)	3.25(38)		
3 $\mathcal{B}_{D^0 \rightarrow K^- e^+ \nu_e}$	37.0	31.8	38.3(2.8)	35.05(36)		
4 $\mathcal{B}_{\bar{B}^0 \rightarrow \pi^+ \ell^- \bar{\nu}_\ell}$	0.41	0.34		0.149(11)		
5 $\mathcal{B}_{B_s^0 \rightarrow K^+ \ell^- \bar{\nu}_\ell}$	0.36	0.29				0.164(17)
6 $\mathcal{B}_{B^0 \rightarrow D^- \ell^+ \nu_\ell}$	25.5	24.0		23.1(1.0)		
7 $\mathcal{B}_{B_s^0 \rightarrow D_s^- \ell^+ \nu_\ell}$	25.0	23.5				24(5)
8 $\mathcal{B}_{B_c^- \rightarrow \eta_c \ell^- \bar{\nu}_\ell}$	8.99	6.65				8.2(1.9)
9 $\mathcal{B}_{B_c^- \rightarrow B^0 \ell^- \nu_\ell}$	1.21	1.20			0.87(5)	1.4(1.0)
10 $\mathcal{B}_{B_c^+ \rightarrow B_s^0 \ell^+ \nu_\ell}$	17.9	18.1			12.6(5)	16(11)

each weak transition vertex possesses a pole at the related meson mass.

The  $D_s^+ \rightarrow K^0$  transition form factors are drawn in Fig. 3. Again, best agreement between the SCI predictions and the results in Ref. [15] is obtained when the complete SCI Bethe-Salpeter amplitude is used. (We quantified this using a  $\mathcal{L}_1$  measure applied to the independent transition form factors  $f_{0,+}$ .) Only one empirical datum is available in this case [29]:

$$f_+^{D_s^+ \rightarrow K^0}(0) = 0.720 \pm 0.084 (\text{stat}) \pm 0.013 (\text{syst}). \quad (43)$$

It is plotted in Fig. 3 and agrees with the SCI result obtained using the complete Bethe-Salpeter amplitude, Fig. 3A.

The  $D \rightarrow K$  transition form factors are drawn in Fig. 4. Best agreement with the predictions from Ref. [15] is obtained using the complete SCI Bethe-Salpeter amplitude, *i.e.* with the  $F_{0^-} \neq 0$  values listed in Table 2. The  $D \rightarrow K$  semileptonic transition form factors in Ref. [15] agree well with available empirical data [28].

With computed transition form factors in hand, one can calculate partial widths for the associated decays. Remaining with  $D \rightarrow \pi$  as our exemplar, the relevant expression is [67]:

$$\Gamma_{D^0 \pi^-} = |V_{cd}|^2 \frac{G_F^2 m_D^2}{24\pi^3} \times \int_0^{y_m^{D\pi}} dy [f_+^{D^d}(y m_D^2)]^2 k_{D\pi}^3(y), \quad (44a)$$

$$k_{D\pi}^2(t) = (m_D^2(1-y) + m_\pi^2)^2 / [4m_D^2] - m_\pi^2, \quad (44b)$$

with  $G_F = 1.166 \times 10^{-5} \text{ GeV}^{-2}$ . Using the SCI results for  $f_+^{D^d}(t)$ , the associated branching fractions are listed in Table 3B: the  $F_{0^-}$  result for this integrated quantity agrees well with other theory [15] and experiment [28].

Analogous SCI results for  $D_s^+ \rightarrow K^0 e^+ \nu_e$ ,  $D^0 \rightarrow K^- e^+ \nu_e$  branching fractions are also listed in Table 3B. Again, those obtained with the complete Bethe-Salpeter amplitude compare favourably with other theory [15] and experiment [28, 29].



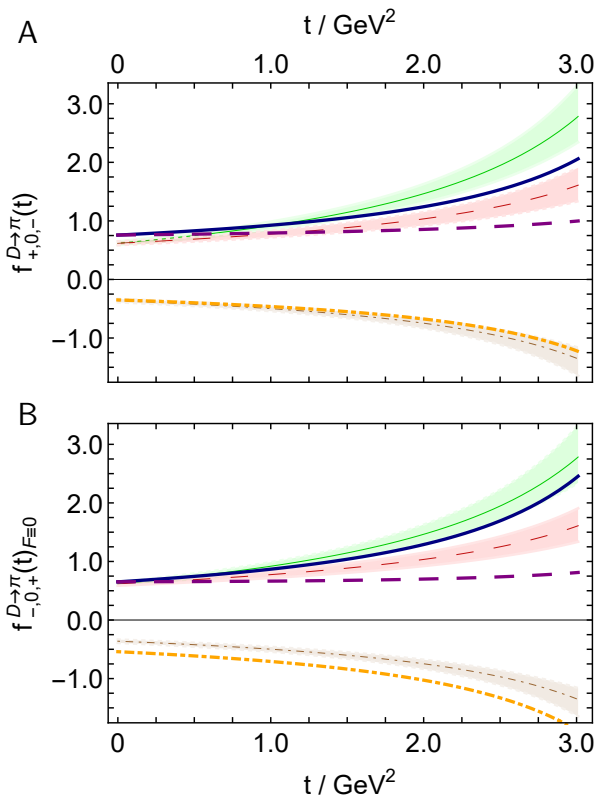


**Fig. 2**  $D \rightarrow \pi$  semileptonic transition form factors, defined by Eqs. (27), (28). SCI results:  $f_{+,0,-}^{D^d}$ , solid blue curve;  $f_0^{D^d}$ , long-dashed purple curve; and  $f_{-,0,+}^{D^d}$ , dot-dashed orange curve. *Upper panel*–A obtained with complete SCI Bethe-Salpeter amplitude in Eq. (13); and *lower panel*–B, with  $F_{0-} \equiv 0$  in Eq. (13) and subsequent repetition of all fitting procedures. Comparison curves in both panels are drawn from Ref. [15]:  $f_+$ , thin solid green curve;  $f_0$ , long-dashed red curve; and  $f_-$ , dot-dashed brown curve. In this and following images, the shaded band around each of the comparison curves indicates the  $1\sigma$  confidence level for these predictions.

## 5 Weak $B_{(c,s)}$ Semileptonic Transitions

Here in the isospin-symmetry limit, there are seven distinct processes, which we choose to be: (i)  $\bar{B}^0 \rightarrow \pi^+$ ,  $B_s \rightarrow K$ ; (ii)  $B^0 \rightarrow D^-$ ,  $B_s^0 \rightarrow D_s^-$ ,  $B_c^- \rightarrow \eta_c$ ; (iii)  $B_c^+ \rightarrow B^0$ ; and (iv)  $B_c^+ \rightarrow B_s^0$ . The first two measure  $b \rightarrow u$  (i); the next three,  $b \rightarrow c$  (ii); the sixth,  $c \rightarrow d$  (iii); and the last,  $c \rightarrow s$  (iv); plus, naturally, their environmental sensitivity. In these cases, no continuum study with the character of Ref. [15] is available; but IQCD methods have been used by many groups, *e.g.* Refs. [59–61, 68, 69], and numerous model studies exist, *e.g.* Refs. [63–66, 70–79].

Results for the maximum-recoil value of all seven of these transition form factors are listed in Table 3A. The SCI and IQCD results are broadly in agreement, except for  $B \rightarrow \pi$  and  $B_s \rightarrow K$  (rows 4 and 5). These last two transitions are special because of the enormous

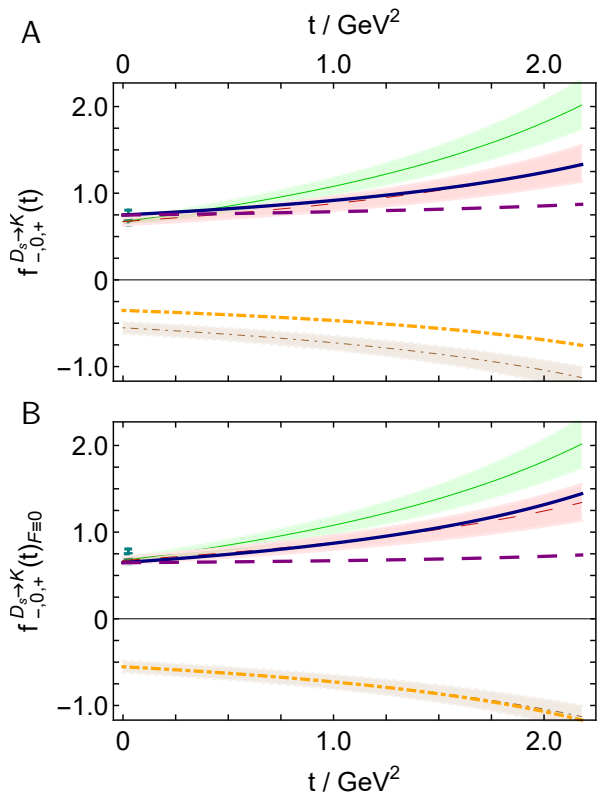


**Fig. 3**  $D_s^+ \rightarrow K^0$  transition form factors, defined by analogy with Eqs. (27), (28). SCI results:  $f_{-,0,+}^{D^d}$ , solid blue curve;  $f_0^{D^d}$ , long-dashed purple curve; and  $f_{-,0,+}^{D^d}$ , dot-dashed orange curve. *Upper panel*–A obtained with complete SCI Bethe-Salpeter amplitude in Eq. (13); and *lower panel*–B, with  $F_{0-} \equiv 0$  and subsequent repetition of all fitting procedures. Comparison curves in both panels are drawn from Ref. [15]:  $f_+$ , thin solid green curve;  $f_0$ , long-dashed red curve; and  $f_-$ , dot-dashed brown curve. Empirical datum, cyan square [29].

disparity in mass-scales between the initial and final states. Surveying a raft of available model analyses [63, 65, 70–77], one finds

$$f_+^{B \rightarrow \pi}(0) = 0.25(3), \quad f_+^{B_s \rightarrow K}(0) = 0.32(4), \quad (45)$$

values consistent with contemporary IQCD estimates. We therefore judge that the SCI results in Table 3A are too large in these two cases. Some failings had to be expected when attempting to develop an internally consistent SCI for use in treating systems with widely separated mass-scales.

Given these last observations, it is worth studying the  $B \rightarrow \pi$  transition form factors in more detail. Therefore, consider Fig. 5, which depicts SCI predictions for their  $t$ -dependence and comparisons with some IQCD results: despite the SCI’s overestimate of the maximum recoil value of  $f_+$ , there is qualitative agreement over the entire physical  $t$ -domain. Using the SCI result in Fig. 5A, one obtains the branching frac-

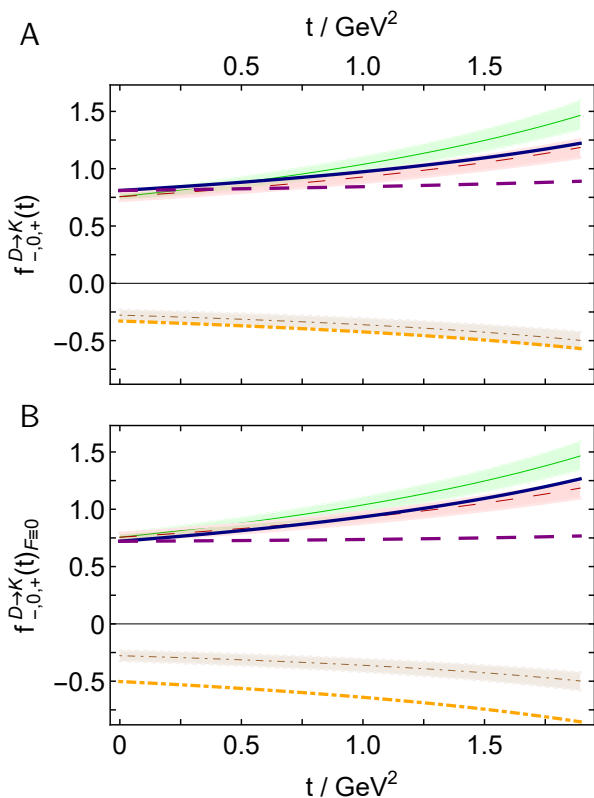


**Fig. 4**  $D \rightarrow K$  transition form factors, defined by analogy with Eqs. (27), (28). SCI results:  $f_{+}^{D_s^s}$ , solid blue curve;  $f_{0}^{D_s^s}$ , long-dashed purple curve; and  $f_{-}^{D_s^s}$ , dot-dashed orange curve. *Upper panel*–A obtained with complete SCI Bethe-Salpeter amplitude in Eq. (13); and *lower panel*–B, with  $F_{0^-} \equiv 0$  and subsequent repetition of all fitting procedures. Comparison curves in both panels are drawn from Ref. [15]:  $f_{+}$ , thin solid green curve;  $f_{0}$ , long-dashed red curve; and  $f_{-}$ , dot-dashed brown curve.

tion listed in Table 3B, row 4: consistent with the overestimate of  $f_{+}(0)$ , the fraction is more than twice as large as the empirical value in Ref. [62]. This indicates that the branching fraction integral is dominated by the transition form factor’s behaviour on  $0 < t \lesssim \frac{2}{3}t_m$ .

$B_s \rightarrow K$  transition form factors are displayed in Fig. 6. The comparison with quenched-IQCD results is qualitatively similar to that in Fig. 5. Using the SCI result in Fig. 6A, one obtains the branching fraction listed in Table 3B, row 5. Here, consistent with the overestimate of  $f_{+}(0)$ , the fraction is roughly twice as large as the model estimates in Refs. [65, 74].

Regarding  $B \rightarrow D$  semileptonic transitions, the mismatch between the masses of the initial and final states is much diminished as compared with the preceding two cases. Consequently, the SCI results drawn in Fig. 7 match fairly well with existing data [81] and recent parametrisations [82]. (*N.B.* Here and hereafter we draw  $|f_{-}(t)|$  so as to optimise use of the plotting area.) The

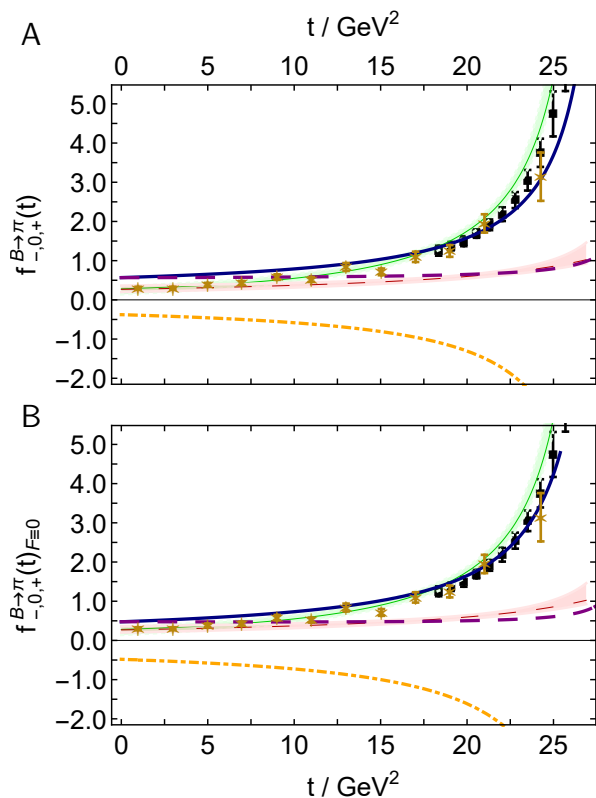


**Fig. 5**  $B \rightarrow \pi$  semileptonic transition form factors, defined by analogy with Eqs. (27), (28). SCI results:  $f_{+}^{B_u^s}$ , solid blue curve;  $f_{0}^{B_u^s}$ , long-dashed purple curve; and  $f_{-}^{B_u^s}$ , dot-dashed orange curve. *Upper panel*–A obtained with complete SCI Bethe-Salpeter amplitude in Eq. (13); and *lower panel*–B, with  $F_{0^-} \equiv 0$  and subsequent refitting. In both panels, the data (gold stars) are from the BaBar Collaboration [80]; the other points (black squares) are IQCD results obtained with  $2 + 1$  flavours of light sea quarks [68]; and the comparison bands are drawn from Ref. [69], being fits to quenched-IQCD calculations.

SCI prediction for the branching fraction is listed in Table 3B, row 6, and aligns with experiment [11, p. 1531].

We depict the SCI  $B_s \rightarrow D_s$  transition form factors in Fig. 8: they agree semiquantitatively with results from a recent IQCD study [59]. The SCI prediction for the branching fraction in Table 3B, row 7, is commensurate with estimates made using constituent quark models [64, 65].

$B_c \rightarrow \eta_c$  transition form factors are plotted in Fig. 9. In this instance, the only comparisons available are provided by exploratory IQCD calculations obtained with a highly improved staggered quark (HISQ) action [60]: there are qualitative similarities between the results. The SCI predictions for the branching fraction are listed in Table 3B, row 8. The values agree with an estimate made using a hybrid scheme for combining perturbative- and lattice-QCD results [66].

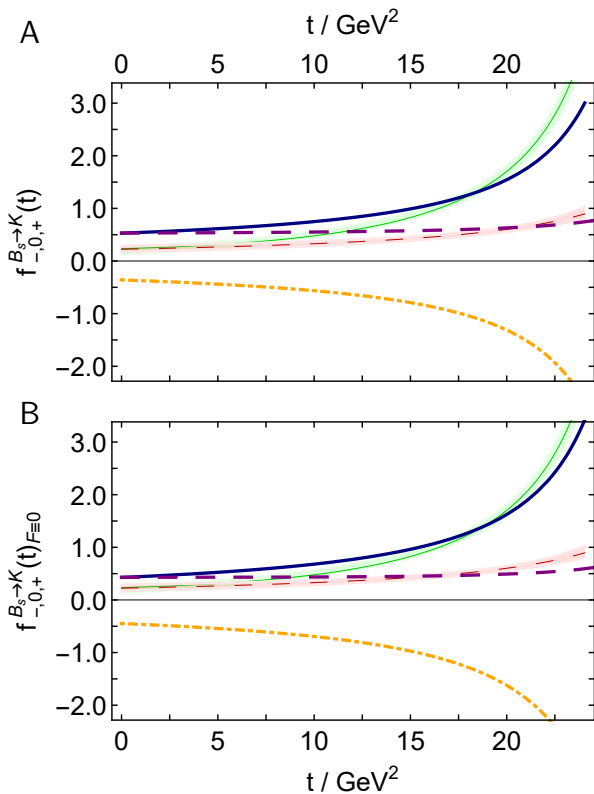


**Fig. 6**  $B_s \rightarrow K$  transition form factors, defined by analogy with Eqs. (27), (28). SCI results:  $f_+^{B_s}$ , solid blue curve;  $f_0^{B_s}$ , long-dashed purple curve; and  $-f_-^{B_s}$ , dot-dashed orange curve. *Upper panel*–A obtained with complete SCI Bethe-Salpeter amplitude in Eq. (13); and *lower panel*–B, with  $F_0 \equiv 0$  and subsequent repetition of all fitting procedures. In both panels, the comparison bands are drawn from Ref. [69], being fits to quenched-IQCD calculations.

SCI predictions for the  $B_c \rightarrow B$  form factors are drawn in Fig. 10, wherein they are compared with IQCD results obtained using  $2 + 1 + 1$  flavours of dynamical sea quarks in the HISQ formalism [61]. As highlighted by Fig. 12, the SCI and IQCD results for  $f_{0,+}$  are qualitatively and semiquantitatively similar, with the SCI curves being approximately 21% larger than those from the IQCD analysis, as measured using a  $\mathcal{L}_1$  measure. The SCI prediction for the  $B_c \rightarrow B$  branching fraction is given in Table 3B, row 9. It fits comfortably within the wide range of model estimates listed in Ref. [63], *viz.*  $1.4(1.0) \times 10^{-3}$ . Using the IQCD results drawn in Fig. 10, we obtain the  $B_c \rightarrow B$  branching fraction listed in Table 3B, row 9, which is approximately 30% smaller than the SCI prediction.

The final weak transition considered herein is  $B_c \rightarrow B_s$ , for which SCI predictions of the associated form factors are drawn in Fig. 11 and compared with IQCD results [61]. As with  $B_c \rightarrow B$ , the SCI and IQCD results for  $f_{0,+}$  are qualitatively and semiquantitatively

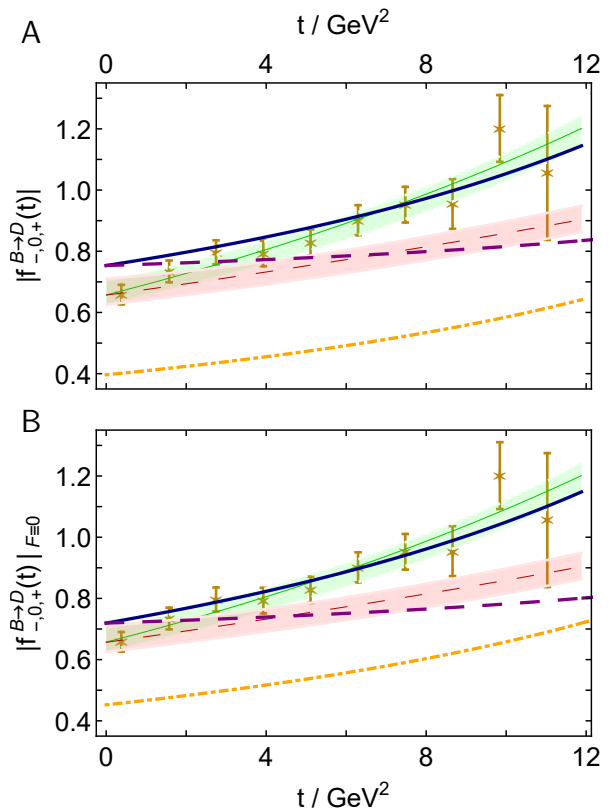


**Fig. 7**  $B \rightarrow D$  transition form factors, defined by analogy with Eqs. (27), (28). SCI results:  $f_+^{B^c}$ , solid blue curve;  $f_0^{B^c}$ , long-dashed purple curve; and  $-f_-^{B^c}$ , dot-dashed orange curve. *Upper panel*–A obtained with complete SCI Bethe-Salpeter amplitude in Eq. (13); and *lower panel*–B, with  $F_0 \equiv 0$  and subsequent repetition of all fitting procedures. In both panels, the data (gold stars,  $f_+$ ) are from the BaBar Collaboration [81]; and the comparison bands (thin dashed red,  $f_0$ ; and thin green,  $f_+$ ) are drawn from Ref. [82], being parametrisations built from recent experimental data and IQCD results.

similar: using a  $\mathcal{L}_1$  measure, the SCI curves are approximately 18% larger than those from the IQCD analysis. This is evident in Fig. 12. The SCI prediction for the associated branching fraction is given in Table 3B, row 10. Once again, it fits within the broad range of model estimates listed in Ref. [63], *viz.*  $16(11) \times 10^{-3}$ . Using the IQCD results drawn in Fig. 11, we obtain the  $B_c \rightarrow B_s$  branching fraction listed in Table 3B, row 10, which is approximately 35% smaller than the SCI prediction.

## 6 Environment Sensitivity

Regarding Nature’s two mass generating mechanisms, it is interesting to consider the evolution of the form factors with increasing mass of the transition’s inactive valence-quark, *i.e.* as the current-quark mass produced by the Higgs boson becomes a more important part

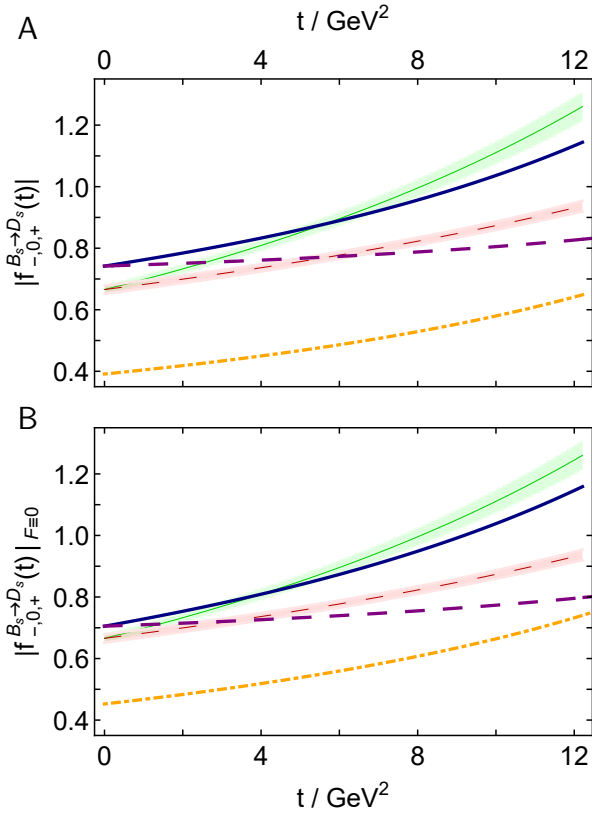


**Fig. 8**  $B_s \rightarrow D_s$  transition form factors, defined by analogy with Eqs. (27), (28). SCI results:  $f_+^{B_s^c}$ , solid blue curve;  $f_0^{B_s^c}$ , long-dashed purple curve; and  $-f_-^{B_s^c}$ , dot-dashed orange curve. *Upper panel*–A obtained with complete SCI Bethe-Salpeter amplitude in Eq. (13); and *lower panel*–B, with  $F_{0^-} \equiv 0$  and subsequent refitting. In both panels, the comparison bands (thin dashed red,  $f_0$ ; and thin green,  $f_+$ ) are drawn from Ref. [59], being IQCD results obtained with inclusion of  $2 + 1 + 1$  flavours of sea quark.

of the final-state meson’s mass as compared with the EHM component. Four classes can be formed from the semileptonic decays considered herein.

- (I)  $D \rightarrow \pi$ ,  $D_s \rightarrow K$ ,  $B_c \rightarrow B$ : transition is  $c \rightarrow d$ ; inactive valence-quarks are, respectively,  $u$ ,  $s$ ,  $b$ .
- (II)  $D \rightarrow K$ ,  $B_c \rightarrow B_s$ : transition  $c \rightarrow s$ , inactive valence-quarks are  $u$ ,  $b$ .
- (III)  $B \rightarrow \pi$ ,  $B_s \rightarrow K$ : transition  $b \rightarrow u$ , inactive valence-quarks are  $d$ ,  $s$ .
- (IV)  $B \rightarrow D$ ,  $B_s \rightarrow D_s$ ,  $B_c \rightarrow \eta_c$ : transition  $b \rightarrow c$ , inactive valence-quarks are  $u$ ,  $s$ ,  $c$ .

One may characterise this evolution by the values of  $[1 - f_+(0)]$  and  $|f_-(0)|$  for the associated transitions:  $[1 - f_+(0)] = 0 = |f_-(0)|$  in systems constituted from mass-degenerate valence degrees-of-freedom. The

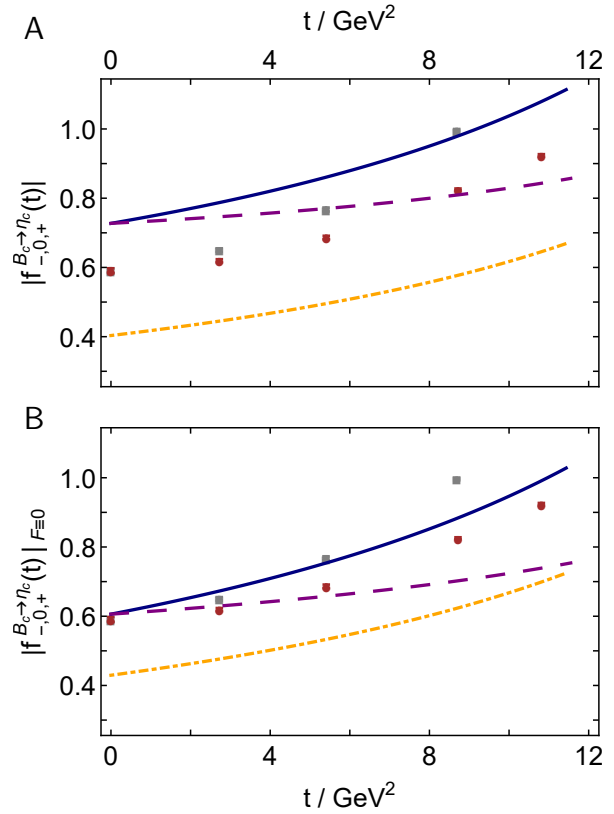


**Fig. 9**  $B_c \rightarrow \eta_c$  transition form factors, defined by analogy with Eqs. (27), (28). SCI results:  $f_+^{B_c^c}$ , solid blue curve;  $f_0^{B_c^c}$ , long-dashed purple curve; and  $-f_-^{B_c^c}$ , dot-dashed orange curve. *Upper panel*–A obtained with complete SCI Bethe-Salpeter amplitude in Eq. (13); and *lower panel*–B, with  $F_{0^-} \equiv 0$  and subsequent refitting. In both panels, the comparison points (brown circles,  $f_0$ ; and grey squares,  $f_+$ ) are drawn from Ref. [60], being exploratory IQCD results.

results can be read from Table 3A:

	$u/d$	$s$	$c$	$b$
(I) $1 - f_+(0)$	0.24	0.25		0.32
$ f_-(0) $	0.35	0.35		0.49
(II) $1 - f_+(0)$	0.19			0.25
$ f_-(0) $	0.33			0.55
(III) $1 - f_+(0)$	0.43	0.47		
$ f_-(0) $	0.38	0.36		
(IV) $1 - f_+(0)$	0.25	0.26	0.27	
$ f_-(0) $	0.40	0.39	0.40	

For comparison, analogous values for  $\pi_{\ell 3}$  and  $K_{\ell 3}$  transitions are, respectively, (1.0, 0.0) and (0.98, 0.087) [14].

The pattern of SCI results is clear: as the current-mass of the inactive valence degree-of-freedom increases, so do deviations from the flavour-symmetry limits. The analysis in Ref. [15], which used similar methods and a realistic quark+antiquark interaction, is too restricted

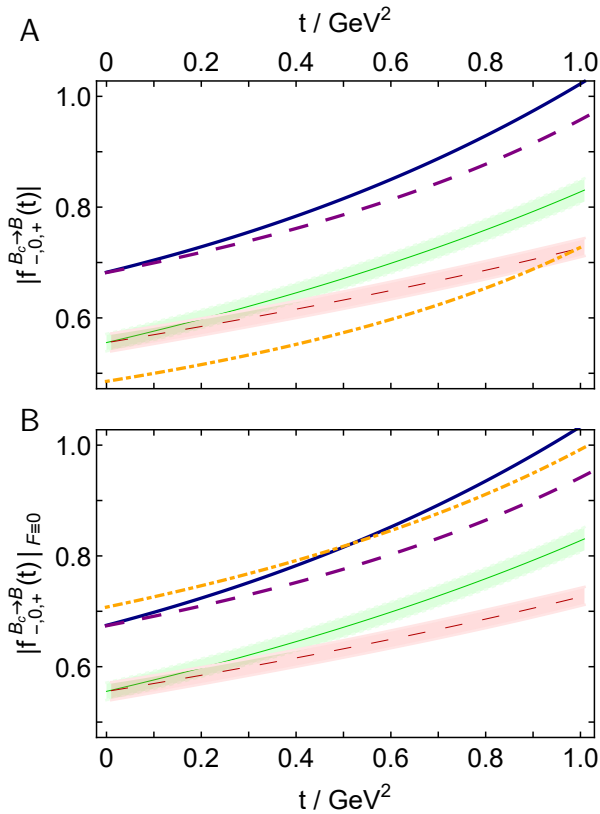


**Fig. 10**  $B_c \rightarrow B$  transition form factors, defined by analogy with Eqs. (27), (28). SCI results:  $f_+^{B_c^d}$ , solid blue curve;  $f_0^{B_c^d}$ , long-dashed purple curve; and  $-f_-^{B_c^d}$ , dot-dashed orange curve. *Upper panel*–A obtained with complete SCI Bethe-Salpeter amplitude in Eq. (13); and *lower panel*–B, with  $F_0 \equiv 0$  and subsequent refitting. In both panels, the comparison bands (thin dashed red,  $f_0$ ; and thin green,  $f_+$ ) are IQCD results from Ref. [61].

in scope for a general comparison to be possible. Nevertheless, the two Class (I) results are loosely compatible.

Lattice-QCD results are available for all listed  $f_+$  form factors, but they are typically from different collaborations. (Class (IV) is something of an exception [61].) Reviewing those simulations, the pattern of IQCD results is nevertheless qualitatively similar to the SCI predictions. However, this is not true for Class (III), *viz.* the  $B \rightarrow \pi$  and  $B_s \rightarrow K$  transitions, which therefore demands further scrutiny.

## 7 Isgur-Wise Function

In considering semileptonic transitions connecting systems distinguished by a large disparity between the current-masses of their valence degrees-of-freedom, *e.g.* heavy+light mesons, valuable simplifications can be exploited. For instance, when  $m_{Q_2} \gtrsim m_{Q_1} \gg m_q$ ,  $H_{Q_2 q} \rightarrow H'_{Q_1 q}$  transitions between heavy+light pseudoscalar me-

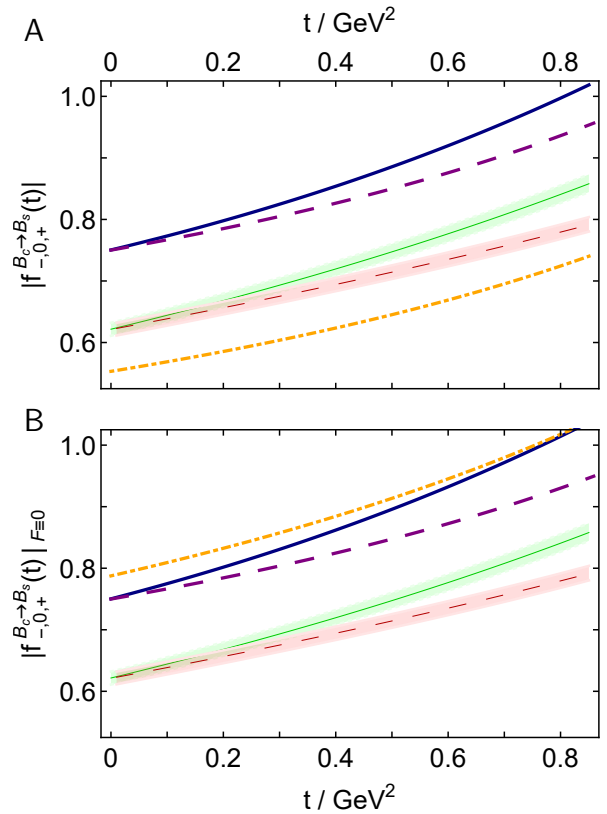


**Fig. 11**  $B_c \rightarrow B_s$  transition form factors, defined by analogy with Eqs. (27), (28). SCI results:  $f_+^{B_c^s}$ , solid blue curve;  $f_0^{B_c^s}$ , long-dashed purple curve; and  $-f_-^{B_c^s}$ , dot-dashed orange curve. *Upper panel*–A obtained with complete SCI Bethe-Salpeter amplitude in Eq. (13); and *lower panel*–B, with  $F_0 \equiv 0$  and subsequent refitting. In both panels, the comparison bands (thin dashed red,  $f_0$ ; and thin green,  $f_+$ ) are IQCD results from Ref. [61].

sons are described by a single, universal function [49]:

$$f_{\pm}^{H \rightarrow H'}(t) = \frac{m_{H'} \pm m_H}{2\sqrt{m_{H'}m_H}} \xi(w(t)), \quad (47a)$$

$$w(t) = \frac{m_{H'}^2 + m_H^2 - t}{2m_{H'}m_H}. \quad (47b)$$

Reviewing the transitions considered herein, two meet the requirements described above, *viz.*  $B \rightarrow D$ ,  $B_s \rightarrow D_s$ ; and in Fig. 13 we depict the function determined from those transition form factors using Eq. (47). Evidently, the SCI produces results that conform with the notions of heavy-quark symmetry: the  $B \rightarrow D$  and  $B_s \rightarrow D_s$  results for  $\xi(w)$  differ by  $< 1\%$  according to a  $\mathcal{L}_1$  measure. Moreover, the SCI prediction for the Isgur-Wise function, although somewhat stiff, is in fair agreement with empirical data [83].

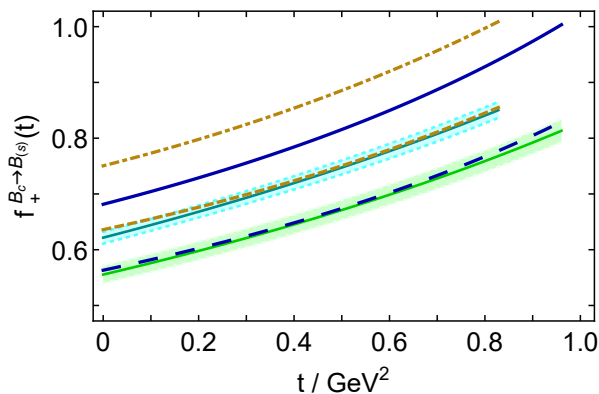


**Fig. 12** SCI predictions for  $f_+^{B_c \rightarrow B}$ , solid blue curve, and  $f_+^{B_c \rightarrow B_s}$ , dot-dashed gold curve, compared with lQCD results for the same functions:  $f_{+ \text{ lQCD}}^{B_c \rightarrow B}$ , thin green curve within like coloured band, and  $f_{+ \text{ lQCD}}^{B_c \rightarrow B_s}$ , thin cyan curve within like coloured band. In addition, calculated from the SCI results,  $f_+^{B_c \rightarrow B}/1.21$ , dashed blue curve, and  $f_+^{B_c \rightarrow B_s}/1.18$ , dot-dashed gold curve. The comparison reveals that, in practical terms on the physical domains, the SCI and lQCD predictions differ only in their overall normalisations, *i.e.* effectively, their respective values for  $f_+(0)$ .

## 8 Summary and Perspective

We employed a symmetry-preserving regularisation of a vector $\times$ vector contact interaction (SCI) to develop a unified treatment of the twelve independent semileptonic transitions involving  $\pi$ ,  $K$ ,  $D_{(s)}$ ,  $B_{(s,c)}$  initial states and the masses and leptonic decays of the fifteen mesons that are either involved in the transitions or characterise the weak transition vertex. The merits of this approach are its algebraic simplicity; paucity of parameters; and simultaneous applicability to such a wide variety of systems and processes, sometimes involving large disparities in mass-scales between initial and final states.

Regarding meson masses, which are long-wavelength properties of the systems, the agreement between SCI predictions and experiment is good [Table 1, Fig. 1], with comparison yielding a mean absolute relative difference  $\overline{\text{ard}} = 3\%$ . Concerning the leptonic decay constants,  $\overline{\text{ard}} = 13\%$ : being dominated by ultraviolet momenta, the decay constants are a greater challenge for the SCI.

Turning to the  $t$ -dependence of transition form factors, the SCI predictions are often somewhat too stiff because the contact-interaction produces momentum-independent meson Bethe-Salpeter amplitudes. Notwithstanding this, wherever experiment or sound theory results are available for comparison, the qualitative behaviour of the SCI results compares well, delivering semiquantitative agreement [Secs. 4, 5]. This is signi-

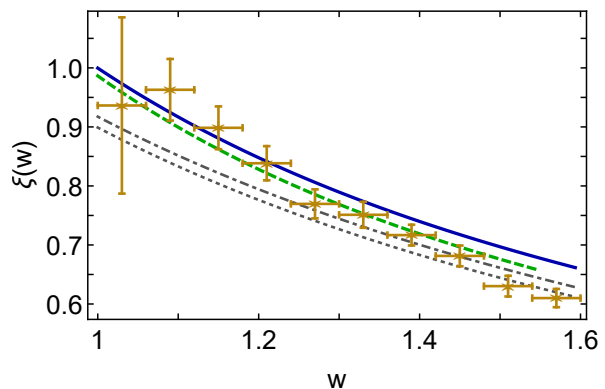


**Fig. 13** SCI predictions for the Isgur-Wise function, Eq. (47), as obtained from the  $B \rightarrow D$  transition, solid blue curve, and the  $B_s \rightarrow D_s$  transition, dashed green curve. Data, gold stars, from Belle Collaboration measurement of  $B \rightarrow D$  [83]. Quark model results obtained from the  $B \rightarrow D$  transition [79]: thin grey dot-dashed (linear potential) and dotted (harmonic oscillator) curves.

ficant because all transitions are treated with the same three SCI-defining parameters. The poorest comparison is found with  $B \rightarrow \pi$  and  $B_s \rightarrow K$ . These transitions, which have huge disparity between mass-scales of the initial and final states, present difficulties for all available methods. Neglecting the  $B \rightarrow \pi$  transition, comparisons between SCI predictions and experimentally measured branching fractions yield  $\overline{\text{ard}} = 7\%$  [Table 3B]. Consequently, the SCI predictions for the five unmeasured branching fractions should be a sound guide.

An additional novel feature of our analysis is the information obtained about the effects that the Higgs mechanism of current-quark mass generation has on the form factors. The suggestion is that as the current-mass of the non-transitioning valence degree-of-freedom increases, so do deviations from the flavour-symmetry limits [Sec. 6].

Considering  $B_{(s)} \rightarrow D_{(s)}$  transitions, we arrived at a prediction for the Isgur-Wise function [Sec. 7]. In comparison with recent  $B \rightarrow D$  data from the Belle Collaboration, the SCI result produces  $\chi^2/\text{datum} = 1.9$ .

Looking forward, it would be natural to use the SCI to unify the pseudoscalar-to-pseudoscalar transitions studied herein with pseudoscalar-to-vector semileptonic transitions. No parameters would need to be introduced or varied; and the results would provide additional benchmarks for analyses based on realistic momentum-dependent interactions. Moreover, our analysis has highlighted a need for the use of symmetry-preserving formulations of realistic interactions in the study of all semileptonic transitions with  $B_{(s,c)}$  initial states. There is a dearth of such theory in this area;

so with this in mind, the approach in Ref. [15] is currently being adapted to unify  $(\pi, K, D, B) \rightarrow \pi$  and  $(D_s, B_s) \rightarrow K$  transitions.

**Acknowledgements** We are grateful for constructive comments from S.-S. Xu, Z.-Q. Yao and P.-L. Yin. Work supported by: National Natural Science Foundation of China (under Grant No. 11805097); Jiangsu Provincial Natural Science Foundation of China (under Grant No. BK20180323).

## References

1. T. Horn, C. D. Roberts, The pion: an enigma within the Standard Model, *J. Phys. G.* 43 (2016) 073001.
2. C. D. Roberts, Empirical Consequences of Emergent Mass, *Symmetry* 12 (2020) 1468.
3. C. D. Roberts, On Mass and Matter, *AAPPS Bulletin* 31 (2021) 6.
4. A. C. Aguilar, et al., Pion and Kaon Structure at the Electron-Ion Collider, *Eur. Phys. J. A* 55 (2019) 190.
5. X. Chen, F.-K. Guo, C. D. Roberts, R. Wang, Selected Science Opportunities for the EicC, *Few Body Syst.* 61 (4) (2020) 43.
6. J.-L. Zhang, K. Raya, L. Chang, Z.-F. Cui, J. M. Morgado, C. D. Roberts, J. Rodríguez-Quintero, Measures of pion and kaon structure from generalised parton distributions, *Phys. Lett. B* 815 (2021) 136158.
7. C. D. Roberts, D. G. Richards, T. Horn, L. Chang, *Insights into the Emergence of Mass from Studies of Pion and Kaon Structure* – arXiv:2102.01765 [hep-ph] .
8. D. P. Anderle, et al., *Electron-Ion Collider in China* – arXiv:2102.09222 [nucl-ex], *Front. Phys. China* (2021) *in press*.
9. J. Arrington, et al., *Revealing the structure of light pseudoscalar mesons at the Electron-Ion Collider* – arXiv:2102.11788 [nucl-ex] .
10. D. Pocanic, et al., Precise measurement of the  $\pi^+ \rightarrow \pi^0 e^+ \nu$  branching ratio, *Phys. Rev. Lett.* 93 (2004) 181803.
11. P. Zyla, et al., Review of Particle Physics, *PTEP* 2020 (2020) 083C01.
12. S. Aoki, et al., FLAG Review 2019, *Eur. Phys. J. C* 80 (2020) 113.
13. C.-R. Ji, P. Maris,  $K_{\ell 3}$  transition form-factors, *Phys. Rev. D* 64 (2001) 014032.
14. C. Chen, L. Chang, C. D. Roberts, S.-L. Wan, S. M. Schmidt, D. J. Wilson, Features and flaws of a contact interaction treatment of the kaon, *Phys. Rev. C* 87 (2013) 045207.
15. Z.-Q. Yao, D. Binosi, Z.-F. Cui, C. D. Roberts, S.-S. Xu, H. S. Zong, Semileptonic decays of  $D_{(s)}$  mesons, *Phys. Rev. D* 102 (2020) 014007.
16. G. Eichmann, H. Sanchis-Alepuz, R. Williams, R. Alkofer, C. S. Fischer, Baryons as relativistic three-quark bound states, *Prog. Part. Nucl. Phys.* 91 (2016) 1–100.
17. V. D. Burkert, C. D. Roberts, Roper resonance: Toward a solution to the fifty-year puzzle, *Rev. Mod. Phys.* 91 (2019) 011003.
18. C. S. Fischer, QCD at finite temperature and chemical potential from Dyson–Schwinger equations, *Prog. Part. Nucl. Phys.* 105 (2019) 1–60.
19. S.-X. Qin, C. D. Roberts, Impressions of the Continuum Bound State Problem in QCD, *Chin. Phys. Lett.* 37 (12) (2020) 121201.
20. H. J. Munczek, Dynamical chiral symmetry breaking, Goldstone’s theorem and the consistency of the Schwinger-Dyson and Bethe-Salpeter Equations, *Phys. Rev. D* 52 (1995) 4736–4740.
21. A. Bender, C. D. Roberts, L. von Smekal, Goldstone Theorem and Diquark Confinement Beyond Rainbow- Ladder Approximation, *Phys. Lett. B* 380 (1996) 7–12.
22. P. Boucaud, J. P. Leroy, A. Le-Yaouanc, J. Micheli, O. Pene, J. Rodríguez-Quintero, The Infrared Behaviour of the Pure Yang-Mills Green Functions, *Few Body Syst.* 53 (2012) 387–436.
23. A. C. Aguilar, D. Binosi, J. Papavassiliou, The Gluon Mass Generation Mechanism: A Concise Primer, *Front. Phys. China* 11 (2016) 111203.
24. M. Q. Huber, Nonperturbative properties of Yang-Mills theories, *Phys. Rept.* 879 (2020) 1 – 92.
25. Z.-F. Cui, J.-L. Zhang, D. Binosi, F. de Soto, C. Mezrag, J. Papavassiliou, C. D. Roberts, J. Rodríguez-Quintero, J. Segovia, S. Zafeiropoulos, Effective charge from lattice QCD, *Chin. Phys. C* 44 (2020) 083102.
26. D. Besson, et al., Improved measurements of D meson semileptonic decays to  $\pi$  and  $K$  mesons, *Phys. Rev. D* 80 (2009) 032005.
27. J. P. Lees, et al., Measurement of the  $D^0 \rightarrow \pi^- e^+ \nu_e$  differential decay branching fraction as a function of  $q^2$  and study of form factor parameterizations, *Phys. Rev. D* 91 (2015) 052022.
28. M. Ablikim, et al., Study of Dynamics of  $D^0 \rightarrow K^- e^+ \nu_e$  and  $D^0 \rightarrow \pi^- e^+ \nu_e$  Decays, *Phys. Rev. D* 92 (2015) 072012.
29. M. Ablikim, et al., First Measurement of the Form Factors in  $D_s^+ \rightarrow K^0 e^+ \nu_e$  and  $D_s^+ \rightarrow K^{*0} e^+ \nu_e$  Decays, *Phys. Rev. Lett.* 122 (2019) 061801.
30. W. Altmannshofer, et al., The Belle II Physics Book, *PTEP* 2019 (12) (2019) 123C01, [Erratum: *PTEP* 2020, 029201 (2020)].
31. C.-Z. Yuan, S. L. Olsen, The BESIII physics programme, *Nature Rev. Phys.* 1 (8) (2019) 480–494.
32. V. Lubicz, L. Riggio, G. Salerno, S. Simula, C. Tarantino, Scalar and vector form factors of  $D \rightarrow \pi(K)\ell\nu$  decays with  $N_f = 2 + 1 + 1$  twisted fermions, *Phys. Rev. D* 96 (2017) 054514, [erratum: *Phys. Rev. D* 99, 099902 (2019)].
33. P. Gambino, et al., Challenges in semileptonic  $B$  decays, *Eur. Phys. J. C* 80 (10) (2020) 966.
34. H. L. L. Roberts, C. D. Roberts, A. Bashir, L. X. Gutiérrez-Guerrero, P. C. Tandy, Abelian anomaly and neutral pion production, *Phys. Rev. C* 82 (2010) 065202.
35. H. L. L. Roberts, A. Bashir, L. X. Gutiérrez-Guerrero, C. D. Roberts, D. J. Wilson,  $\pi^-$  and  $\rho^-$  mesons, and their diquark partners, from a contact interaction, *Phys. Rev. C* 83 (2011) 065206.
36. K.-L. Wang, Y.-X. Liu, L. Chang, C. D. Roberts, S. M. Schmidt, Baryon and meson screening masses, *Phys. Rev. D* 87 (2013) 074038.
37. J. Segovia, I. C. Cloet, C. D. Roberts, S. M. Schmidt, Nucleon and  $\Delta$  elastic and transition form factors, *Few Body Syst.* 55 (2014) 1185–1222.
38. S.-S. Xu, C. Chen, I. C. Cloet, C. D. Roberts, J. Segovia, H.-S. Zong, Contact-interaction Faddeev equation and, *inter alia*, proton tensor charges, *Phys. Rev. D* 92 (2015) 114034.
39. M. A. Bedolla, J. J. Cobos-Martínez, A. Bashir, Charmonia in a contact interaction, *Phys. Rev. D* 92 (2015)

- 054031.
40. M. A. Bedolla, K. Raya, J. J. Cobos-Martínez, A. Bashir,  $\eta_c$  elastic and transition form factors: Contact interaction and algebraic model, *Phys. Rev. D* 93 (2016) 094025.
  41. F. E. Serna, B. El-Bennich, G. Krein, Charmed mesons with a symmetry-preserving contact interaction, *Phys. Rev. D* 96 (2017) 014013.
  42. F. E. Serna-Algarin, Symmetry-preserving contact interaction model for hadron structure and quark matter, Ph.D. thesis, Sao Paulo, IFT, 2017.
  43. K. Raya, M. A. Bedolla, J. J. Cobos-Martínez, A. Bashir, Heavy quarkonia in a contact interaction and an algebraic model: mass spectrum, decay constants, charge radii and elastic and transition form factors, *Few Body Syst.* 59 (2018) 133.
  44. P.-L. Yin, C. Chen, G. Krein, C. D. Roberts, J. Segovia, S.-S. Xu, Masses of ground-state mesons and baryons, including those with heavy quarks, *Phys. Rev. D* 100 (3) (2019) 034008.
  45. L. Gutiérrez-Guerrero, A. Bashir, M. A. Bedolla, E. Santopinto, Masses of Light and Heavy Mesons and Baryons: A Unified Picture, *Phys. Rev. D* 100 (2019) 114032.
  46. P.-L. Yin, Z.-F. Cui, C. D. Roberts, J. Segovia, Masses of positive- and negative-parity hadron ground-states, including those with heavy quarks – arXiv:2102.12568 [hep-ph], *Eur. Phys. J C* (2021) *in press*.
  47. J.-L. Zhang, Z.-F. Cui, J. Ping, C. D. Roberts, Contact interaction analysis of pion GTMDs, *Eur. Phys. J. C* 81 (1) (2021) 6.
  48. Y. Lu, D. Binosi, M. Ding, C. D. Roberts, H.-Y. Xing, C. Xu, Distribution amplitudes of light diquarks, *Eur. Phys. J A (Lett)* (2021) *in press*.
  49. N. Isgur, M. B. Wise, Weak Transition Form Factors between Heavy Mesons, *Phys. Lett. B* 237 (1990) 527–530.
  50. D. Ebert, T. Feldmann, H. Reinhardt, Extended NJL model for light and heavy mesons without  $q\bar{q}$  thresholds, *Phys. Lett. B* 388 (1996) 154–160.
  51. C. D. Roberts, A. G. Williams, G. Krein, On the implications of confinement, *Int. J. Mod. Phys. A* 7 (1992) 5607–5624.
  52. C. D. Roberts, S. M. Schmidt, Reflections upon the Emergence of Hadronic Mass, *Eur. Phys. J. ST* 229 (22-23) (2020) 3319–3340.
  53. N. Mathur, M. Padmanath, S. Mondal, Precise predictions of charmed-bottom hadrons from lattice QCD, *Phys. Rev. Lett.* 121 (20) (2018) 202002.
  54. D. Becirevic, P. Boucaud, J. P. Leroy, V. Lubicz, G. Martinelli, F. Mescia, F. Rapuano, Nonperturbatively improved heavy - light mesons: Masses and decay constants, *Phys. Rev. D* 60 (1999) 074501.
  55. T.-W. Chiu, T.-H. Hsieh,  $B_s$  and  $B_c$  mesons in lattice QCD with exact chiral symmetry, PoS LAT2006 (2007) 180.
  56. B. Colquhoun, C. T. H. Davies, R. J. Dowdall, J. Kettle, J. Koponen, G. P. Lepage, A. T. Lytle, B-meson decay constants: a more complete picture from full lattice QCD, *Phys. Rev. D* 91 (2015) 114509.
  57. D. Binosi, et al., Distribution Amplitudes of Heavy-Light Mesons, *Phys. Lett. B* 790 (2019) 257–262.
  58. M. Chen, M. Ding, L. Chang, C. D. Roberts, Mass-dependence of pseudoscalar meson elastic form factors, *Phys. Rev. D* 98 (2018) 091505(R).
  59. E. McLean, C. T. H. Davies, J. Koponen, A. T. Lytle,  $B_s \rightarrow D_s \ell \nu$  Form Factors for the full  $q^2$  range from Lattice QCD with non-perturbatively normalized currents, *Phys. Rev. D* 101 (2020) 074513.
  60. B. Colquhoun, C. Davies, J. Koponen, A. Lytle, C. McNeile,  $B_c$  decays from highly improved staggered quarks and NRQCD, PoS LATTICE2016 (2016) 281.
  61. L. J. Cooper, C. T. H. Davies, J. Harrison, J. Komijani, M. Wingate,  $B_c \rightarrow B_{s(d)}$  form factors from lattice QCD, *Phys. Rev. D* 102 (2020) 014513.
  62. A. Sibidanov, et al., Study of Exclusive  $B \rightarrow X_u \ell \nu$  Decays and Extraction of  $|V_{ub}|$  using Full Reconstruction Tagging at the Belle Experiment, *Phys. Rev. D* 88 (3) (2013) 032005.
  63. D. Ebert, R. N. Faustov, V. O. Galkin, Weak decays of the  $B_c$  meson to  $B_s$  and  $B$  mesons in the relativistic quark model, *Eur. Phys. J. C* 32 (2003) 29–43.
  64. S.-M. Zhao, X. Liu, S.-J. Li, Study on  $B_s \rightarrow D_{s,J}(2317, 2460) \ell \bar{\nu}_l$  Semileptonic Decays in the CQM Model, *Eur. Phys. J. C* 51 (2007) 601–606.
  65. R. N. Faustov, V. O. Galkin, Weak Decays of  $B_s$  Mesons, in: Helmholtz International Summer School on Physics of Heavy Quarks and Hadrons, 62–72, 2014.
  66. X.-Q. Hu, S.-P. Jin, Z.-J. Xiao, Semileptonic decays  $B_c \rightarrow (\eta_c, J/\psi) \ell \bar{\nu}_l$  in the “PQCD + Lattice” approach, *Chin. Phys. C* 44 (2) (2020) 023104.
  67. B. Bajc, S. Fajfer, R. J. Oakes, An Effective model for charmed meson semileptonic decays, *Phys. Rev. D* 53 (1996) 4957–4963.
  68. J. A. Bailey, et al., The  $B \rightarrow \pi \ell \nu$  semileptonic form factor from three-flavor lattice QCD: A Model-independent determination of  $|V_{ub}|$ , *Phys. Rev. D* 79 (2009) 054507.
  69. A. Al-Haydari, A. Ali Khan, V. M. Braun, S. Collins, M. Gockeler, G. N. Lacagnina, M. Panero, A. Schäfer, G. Schierholz, Semileptonic form factors  $D \rightarrow \pi, K$  and  $B \rightarrow \pi, K$  from a fine lattice, *Eur. Phys. J. A* 43 (2010) 107–120.
  70. D. Melikhov, N. Nikitin, S. Simula, Rare exclusive semileptonic  $b \rightarrow s$  transitions in the standard model, *Phys. Rev. D* 57 (1998) 6814–6828.
  71. D. Melikhov, Dispersion approach to quark binding effects in weak decays of heavy mesons, *Eur. Phys. J. direct C* 4 (2002) 1–154.
  72. A. Faessler, T. Gutsche, M. A. Ivanov, J. Körner, V. E. Lyubovitskij, The Exclusive rare decays  $B \rightarrow K(K^*) \bar{\ell} \ell$  and  $B_c \rightarrow D(D^*) \bar{\ell} \ell$  in a relativistic quark model, *Eur. Phys. J. direct C* 4 (2002) 18.
  73. P. Ball, R. Zwicky, New results on  $B \rightarrow \pi, K, \eta$  decay form factors from light-cone sum rules, *Phys. Rev. D* 71 (2005) 014015.
  74. Y.-L. Wu, M. Zhong, Y.-B. Zuo,  $B_{(s)}, D_{(s)} \rightarrow \pi, K, \eta, \rho, K^*, \omega, \phi$  Transition Form Factors and Decay Rates with Extraction of the CKM parameters  $|V_{ub}|, |V_{cs}|, |V_{cd}|$ , *Int. J. Mod. Phys. A* 21 (2006) 6125–6172.
  75. A. Khodjamirian, T. Mannel, N. Offen, Form-factors from light-cone sum rules with B-meson distribution amplitudes, *Phys. Rev. D* 75 (2007) 054013.
  76. C.-D. Lü, W. Wang, Z.-T. Wei, Heavy-to-light form factors on the light cone, *Phys. Rev. D* 76 (2007) 014013.
  77. M. A. Ivanov, J. G. Körner, S. G. Kovalenko, C. D. Roberts, B- to light-meson transition form factors, *Phys. Rev. D* 76 (2007) 034018.
  78. X.-Q. Hu, S.-P. Jin, Z.-J. Xiao, Semileptonic decays  $B/B_s \rightarrow (D^{(*)}, D_s^{(*)}) \ell \nu_l$  in the PQCD approach with the lattice QCD input, *Chin. Phys. C* 44 (5) (2020) 053102.
  79. H.-M. Choi, *Self-consistent light-front quark model analysis of  $B \rightarrow D \ell \nu_\ell$  transition form factors* – arXiv:2102.02015 [hep-ph] .
  80. B. Aubert, et al., Measurement of the  $B^0 \rightarrow \pi^- \ell^+ \nu$  form-factor shape and branching fraction, and determi-



- 
- nation of  $|V_{ub}|$  with a loose neutrino reconstruction technique, Phys. Rev. Lett. 98 (2007) 091801.
81. B. Aubert, et al., Measurement of  $|V_{cb}|$  and the Form-Factor Slope in  $\bar{B} \rightarrow D\ell\bar{\nu}_\ell$  Decays in Events Tagged by a Fully Reconstructed  $B$  Meson, Phys. Rev. Lett. 104 (2010) 011802.
  82. D.-L. Yao, P. Fernandez-Soler, F.-K. Guo, J. Nieves, New parametrization of the form factors in  $\bar{B} \rightarrow D\ell\bar{\nu}_\ell$  decays, Phys. Rev. D 101 (3) (2020) 034014.
  83. R. Glattauer, et al., Measurement of the decay  $B \rightarrow D\ell\nu_\ell$  in fully reconstructed events and determination of the Cabibbo-Kobayashi-Maskawa matrix element  $|V_{cb}|$ , Phys. Rev. D 93 (3) (2016) 032006.